Atmospheric Research 334 (2026) 108748

Contents lists available at ScienceDirect

Atmospheric Research

journal homepage: www.elsevier.com/locate/atmosres

Case study of aircraft icing in-cloud measurements and explicit supercooled water prediction in Eastern China

Liping Luo [a,b,*], Ming Xue [c], Xin Xu [d], Lin Deng [b], Junxia Li [e], Rong Zhang [e]

[a] College of Civil Aviation, Nanjing University of Aeronautics and Astronautics, Nanjing 211106, China
[b] Shanghai Typhoon Institute, China Meteorological Administration, Shanghai 200030, China
[c] Center for Analysis and Prediction of Storms and School of Meteorology, University of Oklahoma, Norman, OK 73072, USA
[d] Key Laboratory of Mesoscale Severe Weather/Ministry of Education and School of Atmospheric Sciences, Nanjing University, Nanjing 210023, China
[e] China Meteorological Administration Weather Modification Centre, Beijing 100081, China

ARTICLE INFO

Keywords:
Aircraft icing
Microphysics scheme
Numerical simulation
Explicit supercooled water prediction

ABSTRACT

In the morning of 12 November 2022, severe aircraft icing occurred over Anhui Province, Eastern China during weather modification operations. In-situ airborne measurements revealed the presence of a substantial concentration of supercooled droplets with effective diameter exceeding 45 μm, and liquid water content (LWC) above 1.2 g m^{-3} during the icing event.

Given the importance of microphysical parameterization (MP) scheme for icing conditions, simulations using different multi-moment MP schemes, i.e., WDM6, NSSL, Milbrandt-Yau (MY) schemes, are conducted at 1-km grid spacing for the case. Comparisons against satellite observations indicate that the general evolution of the frontal system and surface precipitation are well reproduced by the simulations. However, all simulations underpredict upper-level clouds with cloud-top temperature below 240 K over the northeastern part of the front. Besides, WDM6 scheme produces ice cloud-top area (CTA) closest to satellite observations but only produces approximately half of the observed CTA for supercooled cloud tops. The Milbrandt-Yau scheme shows superior performance in simulating the cloud top features during the icing event. Examinations of explicit supercooled cloud water (SCW) prediction skills indicate that WDM6 generates excessive total number concentration (*Nt*) of small SCW, with *Nt* reaching up to 10^{11} m^{-3} and effective diameter (*ED*) below 20 μm. In contrast, the NSSL scheme produces significantly larger SCW particles but substantially lower *Nt* at approximately 10^{7} m^{-3} and *ED* of above 200 μm. Notably, the particle size distribution of SCW predicted by MY scheme is more realistic compared with in-situ aircraft measurements.

1. Introduction

Aircraft icing occurs when supercooled liquid water freezes on any part of the external structure of an aircraft during flight. Meteorological factors, such as the liquid water content (LWC), temperature, and the sizes of the impinging supercooled liquid water (SLW), particularly supercooled large droplets (SLD, with diameter larger than 50 μm) are critical in determining icing probability and severity (Yamazaki et al., 2021). Aircraft icing can significantly degrade flight performance by altering the aircraft's aerodynamic shape. In less severe cases, icing affects stability and maneuverability, while in severe cases, it can cause communication disruptions, loss of lift, aircraft stalls and loss of control. Furthermore, analyses of the National Transportation Safety Board (NTSB) database (1989–2008) and the Federal Aviation Administration (FAA) Accident/Incident Data System (AIDS) database (1985–2006), revealed that icing-related accidents account for approximately 5 % to 10 % of total aviation incidents. Notably, 25 % to 54 % of these icing-related accidents involved fatalities (e.g., Reveley et al., 2014; Gultepe et al., 2019). Notably, according to the Development and Market Outlook of China's General Aviation Industry, the number of general aviation aircrafts has surged, exceeding that of civil aviation aircrafts by 2021. However, these aircrafts typically operate at lower altitudes and speeds, often within clouds, and frequently lack anti-icing devices. This has led to severe icing-related accidents, such as the crashes of a training aircraft in January 2020 and a cloud-seeding aircraft in March 2021 in China. Therefore, in-depth understanding of cloud microphysical

* Corresponding author at: College of Civil Aviation, Nanjing University of Aeronautics and Astronautics, Nanjing 211106, China.
E-mail address: lpingluo@nuaa.edu.cn (L. Luo).

https://doi.org/10.1016/j.atmosres.2026.108748
Received 11 June 2025; Received in revised form 4 January 2026; Accepted 4 January 2026
Available online 5 January 2026

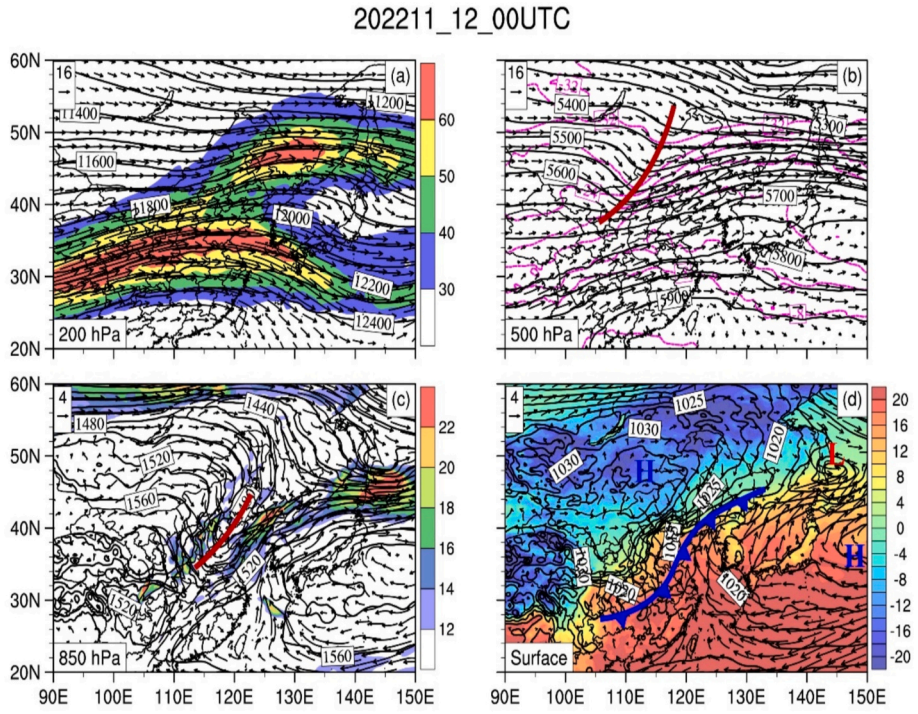

Fig. 1. Synoptic features of the aircraft icing event at 0000 UTC 12 November 2022, at the levels of (a) 200, (b) 500, and (c) 850 hPa from ERA5 reanalysis, showing geopotential height (gpm) in solid black contours, wind vectors (m s^{-1}) in black arrows. The total horizontal wind speed (shaded, m s^{-1}) is shown in panels (a) and (c), and the magenta solid lines in (b) denote the air temperature at 4 °C intervals. In panel (d), temperature at 2-m height above the ground is shaded and the black solid contours denote the mean sea level pressure at 2.5-hPa intervals. The corresponding black arrows indicate the horizontal winds at 10-m height above the ground. The brown and blue solid lines in (b-c) and (d) denote the trough and the cold front, respectively. The uppercase L and H indicates the high and low pressure of the saddle-field at low level over eastern China. (For interpretation of the references to colour in this figure legend, the reader is referred to the web version of this article.)

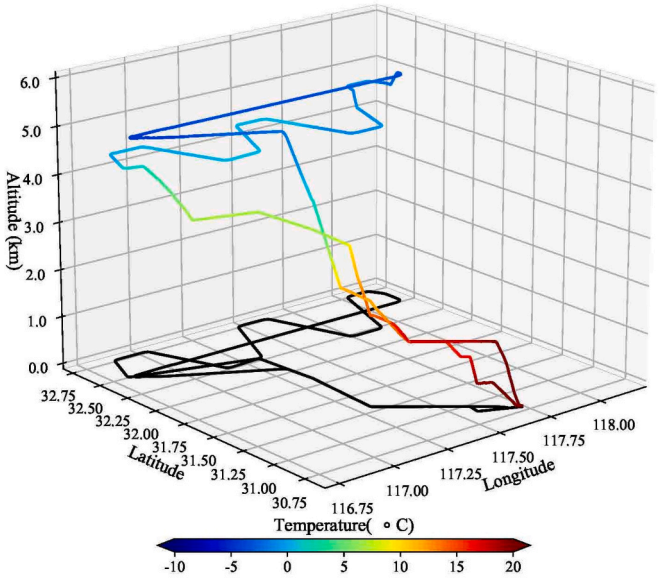

Fig. 2. Three-dimensional flight path colored with air temperature during the icing event on November 122,022. The black solid line indicates the flight path projection on the surface.

properties and improved prediction of SLW are essential for flight safety.

Observations of aircraft icing cloud properties and the formation mechanisms of supercooled water have been an important research topic over the recent decades. In early 1990s, in-cloud aircraft measurements were conducted to detect SLD in western Colorado (e.g., Rasmussen et al., 1992) and the Great Lakes region (e.g., Miller et al., 1998), and the impacts of SLD on aircraft performance were examined. In southern Quebec and Newfoundland, field campaigns on winter storms and freezing rain, i.e., the Canadian Atlantic Storms Program (CASP) (Stewart, 1991; Cober et al., 1995), the First and Third Canadian Freezing Drizzle Experiments (CFDE I and III) (Isaac et al., 1999, 2001) were also conducted to deepen the understanding of cloud microphysical characteristics and SLW distribution under various environmental conditions. More recently, the In-cloud Icing and Large drop Experiment (ICICLE) international field campaign was conducted over the western Great Lakes region in the central United States, to further advance the understanding of meteorological processes related to the production of SLW, with a particular emphasis on SLD (Bernstein et al., 2021). Observational technology in China has also been developed rapidly, with airborne cloud particle probes serving as crucial tools for cloud microphysics observations. Based on airborne in-cloud measurements, satellite and radar observations, Sun et al. (2019) analyzed the microphysical properties of icing clouds over Anhui Province, China. More recently, the atmospheric condition and cloud microphysical features during an aircraft icing event in Shanxi Province, China were analyzed in Wang et al. (2022a), aiming to support the site selection for natural icing test flights of the China-made C919 passenger jet. However, understanding of cloud microphysical properties related to aircraft icing in China, including the spatial and temporal distribution of SLW and its corresponding particle size distributions (PSDs), remains rather limited. In addition, observations also indicate that significant differences exist in cloud properties associated with icing across various regions with different atmospheric conditions (e.g., Yum and Hudson, 2002; Cober and Isaac, 2012; Grosvenor et al., 2012; Listowski et al., 2019).

Forecasting the regions of aircraft icing risk and its severity still pose significant challenges for operational meteorologists (e.g., Tessendorf et al., 2021; Jensen et al., 2023; Kim et al., 2024a). Traditionally,

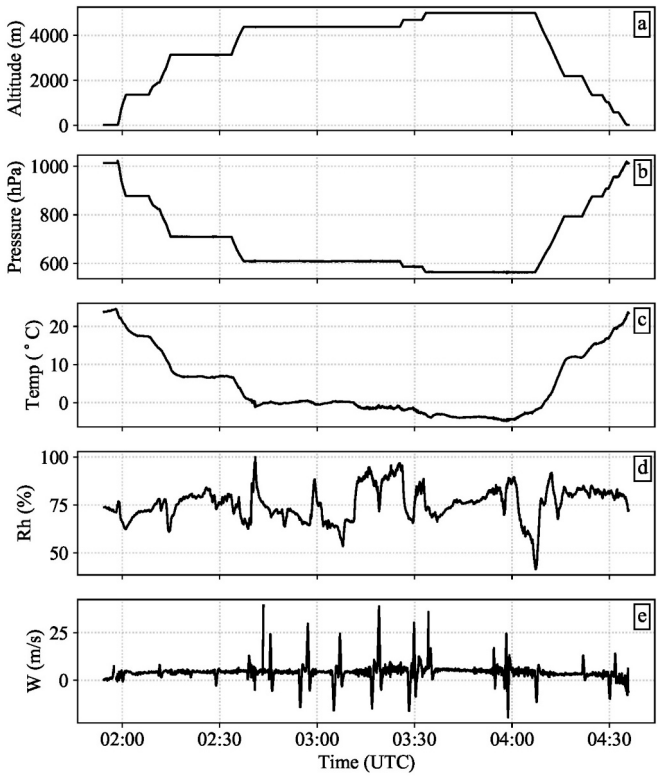

Fig. 3. Environmental condition measured by Aircraft-Integrated Meteorological Measurement System (AIMMS) between 0154 and 0435 UTC on November 122,022, including time series of (a) the flight altitude (m), (b) atmospheric pressure (hPa), (c) temperature (°C), (d) relative humidity (%), and (e) aircraft relative vertical wind speed (m s^{-1}).

aircraft icing prediction has primarily relied on various icing indices, including the RAP, RAOB and IC indices (e.g., Schultz and Politovich, 1992; Thompson et al., 1997). These indices are calculated based on the environmental conditions such as atmospheric temperature, humidity, and stability. However, evaluations have indicated that these icing indices tend to significantly overestimate the extent of icing, and the forecast icing may occur inexplicably even in cloud-free regions (Cornell et al., 1995). Further refinements have been made through satellite and radar observations, as well as pilot reports, leading to the development of the Current Icing Potential (CIP) and Forecast Icing Potential (FIP) algorithms. The FIP provides icing forecasts based on the thermodynamic and water-phase data from NOAA/NCEP's Rapid Refresh (RAP) model (Bernstein et al., 2005). Thus, if the NWP models can accurately predict the evolution of thermodynamic and moisture variables, then the direct prediction of icing will become more advantageous (Thompson et al., 2017).

However, many previous studies have noted that various properties of the simulated clouds are sensitive to the microphysics parameterization (MP) schemes and significant uncertainties exist in modeling supercooled water related microphysical processes (e.g., Dawson et al., 2010; Loftus et al., 2014; Luo et al., 2018, Luo et al., 2021; Ma et al., 2021). For example, based on a set of aircraft icing events with in-cloud microphysical measurements, high sensitivity of the predicted LWC to MP schemes were revealed in Merino et al. (2019). Previous studies have also highlighted that the icing intensity, as quantified by IC index, exhibits pronounced sensitivity to MP schemes (Guo et al., 2023). Jensen et al. (2023) evaluated the predicted SLD by the Thompson-Eidhammer (TE) scheme of the High-Resolution Rapid Refresh (HRRR) model using observations from the ICICLE field campaign. It was found that the TE scheme predicted a much lower concentration of SLD compared with observations over North America. These discrepancies may primarily be attributed to uncertainties in the calculation of microphysical processes associated with supercooled water within MP schemes. More recently, Yuan et al. (2025) analyzed cloud microphysical properties and processes for two inflight icing events over the Sichuan Basin, utilizing in-situ aircraft measurements and model simulations. To our knowledge, detailed evaluations of the modeled PSDs of SLW have not been conducted for icing cases in China.

In this study, we focus on a severe aircraft icing event over Eastern China on November 12, 2022. The goals of this study are two-fold. Firstly, the microphysical structures of the icing event are investigated using airborne in-situ measurements and the Nanjing Joint Institute for Atmospheric Sciences (NJIAS) Himawari-8/9 Cloud Feature Dataset (HCFD) (Zhuge et al., 2024) over Eastern China. Secondly, sensitivity simulations using various commonly used multi-moment MP schemes, including WDMS6, NSSL, and MY schemes at 1-km resolution are conducted for the icing event. The cloud microphysical properties, explicit prediction skills of SLW, especially the PSDs of SLW from the simulations using various multi-moment MP schemes are examined.

The remainder of this paper is organized as follows. Section 2 provides an overview of the aircraft icing event to be studied and the corresponding observational datasets. Section 3 documents the configurations of the numerical experiments. Evaluation metrics for cloud-top properties and supercooled water are present in Section 4. Results including airborne in-situ observations, evaluations of MP schemes in terms of cloud properties and the corresponding explicit prediction skills of SLW are shown in Section 5. Finally, a summary and conclusions are present in Section 6.

2. Case overview and observational datasets

2.1. Overview of the aircraft icing event

On November 12, 2022, an aircraft icing event occurred over Anhui Province China during weather modification operations, within stratocumulus clouds above a strong cold front that had moved southeastward, reaching the eastern part of China. Such situations frequently lead to severe aircraft icing in winter in this region (e.g., Sun et al., 2019).

Fig. 1 illustrates the synoptic features of this event at 00 UTC on November 122,022, approximately two hours before the aircraft takes off, based on the fifth-generation ECMWF reanalysis (ERA5; Hersbach et al., 2020) at $0.25^{o} \times 0.25^{o}$ resolution. At that time, northeastern China was situated beneath a strong high-level jet and a mid-level East Asian trough (EAT), accompanied by strong cold advection that favored the deepening of the EAT at 500 hPa (Figs. 1a, b). At 850 hPa, an elongated northeast-southwest oriented trough extended from north of the Korean Peninsula to eastern China, with Anhui Province located beneath the bottom of the trough. Ahead of the trough, a strong low-level jet developed (Fig. 1c). Previous studies (e.g., Ellrod and Bailey, 2007; Bernstein et al., 2019; Sun et al., 2019; Wang et al., 2022b) have noted that the convergence and lifting of abundant warm and moist air ahead of the low-level trough, associated with a frontal system, favor the genesis of supercooled liquid water. At the surface, a distinct saddle-field developed, characterized by a deformation region with relatively calm winds, surrounded by the cold continental high, subtropical high, and two low pressure systems over northeastern Japan and the southwestern part of China, respectively (Fig. 1d). The unique saddle flow pattern often leads to the development of the cold front and intense precipitation due to the associated flow convergence (e.g., Gao et al., 2008; Wu et al., 2010; Wang, 2023). Above all, the southeastward-moving strong cold front and the low-level southwesterly jet transporting warm and moist air over Anhui Province, synergistically supported the formation of supercooled liquid water in the developed stratocumulus clouds that caused aircraft icing.

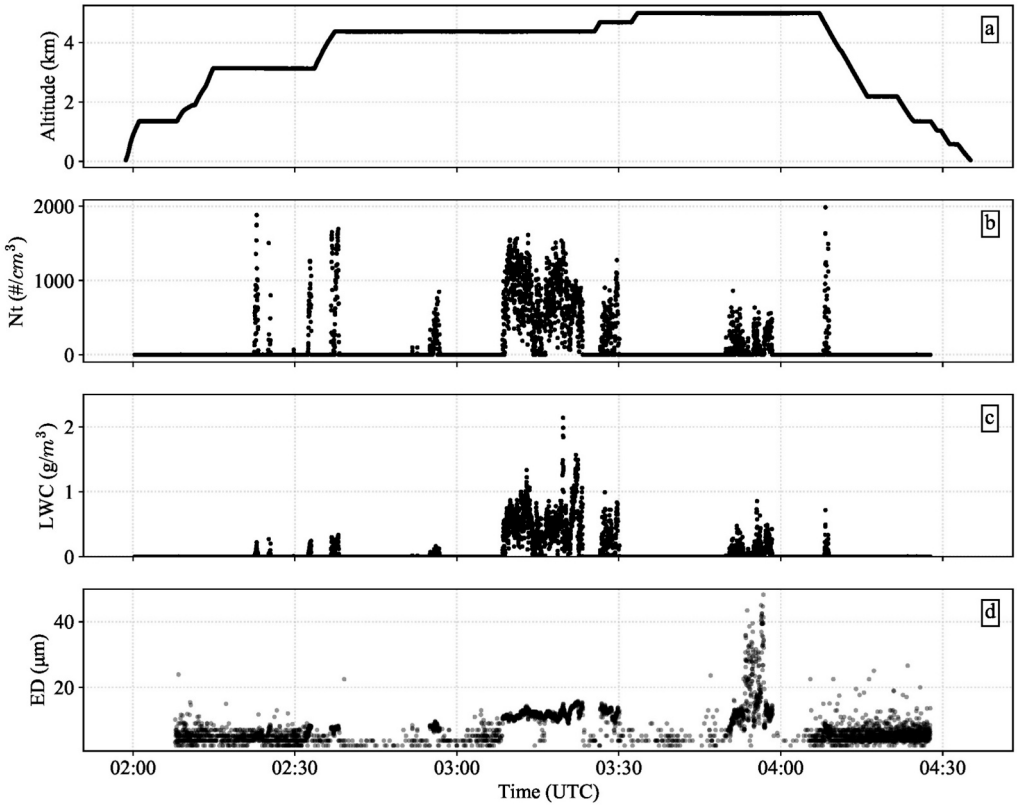

Fig. 4. Measurement of cloud droplet by the fast cloud droplet probe (FCDP), including (a) the altitude (m), (b) total cloud droplet number concentration (#/cm^3), (c) liquid water content (g m^{-3}), and (d) effective diameter of cloud droplet (μm) between 0154 and 0435 UTC on November 122,022.

2.2. *In-situ aircraft measurements and satellite observations*

The observations used in this study include both in-situ aircraft measurements and satellite retrieval datasets. On that day, the aircraft conducted cloud penetration observation over central Anhui Province, equipped with a comprehensive suite of instruments. Fig. 2 presents the three-dimensional flight path colored with observed ambient temperature during the in-situ observation. The Aircraft Integrated Meteorological Measurement System (AIMMS-20) was deployed to measure meteorological variables including atmospheric temperature, relative humidity, barometric pressure, three-dimensional wind component (*u/v/w*), and GPS positioning data. Additionally, the high-resolution Ka-Band Precipitation Cloud Radar (KPR) was utilized to detect precipitation and the microphysical structure within clouds. The radar beam was configured to scan vertically along the flight path, enabling multi-directional cloud observation. A Fast Cloud Droplet Probe (FCDP) measured the shape, size and number concentration of liquid and ice particles with diameters ranging from 2 to 50 μm across 21 standard size bins. Both liquid water content (LWC) data retrieved from the FCDP and measurements from the Nevzorov hot-wire LWC/TWC probe were analyzed. However, since the Nevzorov hot-wire LWC/TWC probe malfunctioned during the flight (with TWC values fixed at 0.003 g/m^3), the LWC values reported in this study were derived exclusively from the FCDP. We acknowledge that the FCDP-derived LWC may be underestimated due to its inability to detect droplets with diameters exceeding 50 μm. We will collect additional aircraft-based in-situ observations to better analyze the characteristics of SLW in future research.

The primary satellite dataset employed for model evaluation is the Nanjing Joint Institute for Atmospheric Sciences (NJIAS) Himawari-8/9 Cloud Feature Dataset (HCFD) at a spatial resolution of 0.04^o and a temporal resolution of 30 min. HCFD encompasses 26 variables and provides comprehensive cloud properties over East Asia and the west North Pacific. Validation against other satellite observations demonstrates that multiple cloud variables in the NJIAS HCFD exhibit superior performance compared to the Japanese operational Himawari-8/9 cloud products (Zhuge et al., 2024). Cloud products utilized in this study include cloud-top thermodynamic phase, cloud-top height, cloud-top temperature. Additionally, simulated precipitation is compared with half-hourly precipitation estimates from the final run of the Integrated Multi-satellite Retrievals for Global Precipitation Measurement (IMERG-F) at 0.1^o spatial resolution (Huffman et al., 2023).

3. Configurations of numerical experiments

Simulations of the aircraft icing event were conducted using the Advanced Research Weather Research and Forecasting (WRF) model version 4.3.1 (Skamarock et al., 2019). Three one-way nested domains at 9-km, 3-km and 1-km horizontal grid spacings were employed. The innermost domain covered both Anhui and Jiangsu Provinces with 601 × 601 grid points (Fig. 6). The domains had 61 hybrid vertical coordinate (HVC) levels extending from the surface to 10 hPa. These levels utilized a terrain-following (TF) coordinate near the ground and transitioned to isobaric levels at a predefined default altitude of about 12 km. The default altitude which determines the transition from TF to HVC coordinates, was deemed globally applicable and robust based on prior tests (Beck et al., 2020; Skamarock et al., 2019). All domains were initialized at 1200 UTC November 11 and integrated until 0000 UTC November 13, encompassing most of the lifecycle of the frontal system and the entire aircraft flight segments. The ERA5 reanalysis datasets (0.25^o × 0.25^o resolution, 1-h intervals) were used as the initial and boundary conditions, respectively for the simulations. Previous studies have demonstrated that WRF model forced by ERA5 reanalysis, exhibits higher accuracy in simulating surface wind and precipitation compared to ERA-interim (Duzenli et al., 2021; Wei et al., 2023; Xu et al., 2024).

The YSU planetary boundary layer scheme (Hong et al., 2006) was employed to parameterize the vertical diffusion of heat and moisture

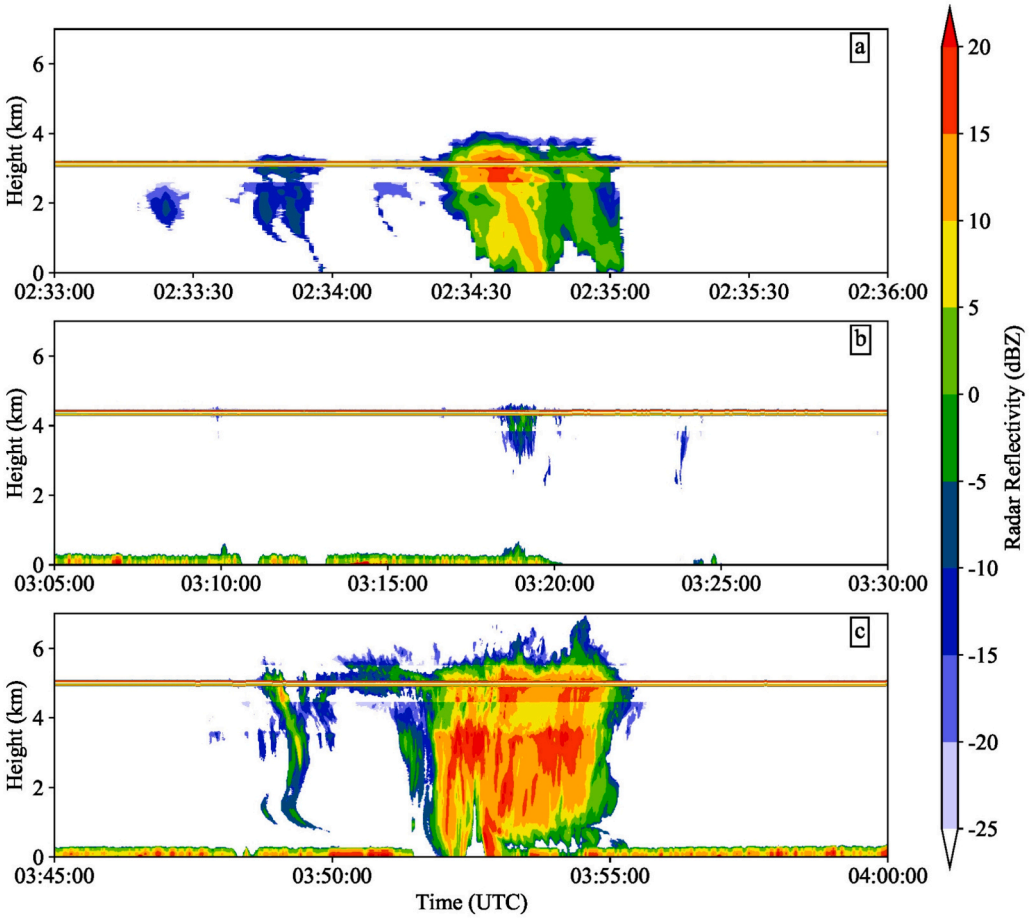

Fig. 5. Radar reflectivity (dBZ) observed by the Ka-band cloud radar during three segments of the flight, i.e., (a) 0233–0236, (b) 0305–0330 and (c) 0345–0400 UTC on November 122,022.

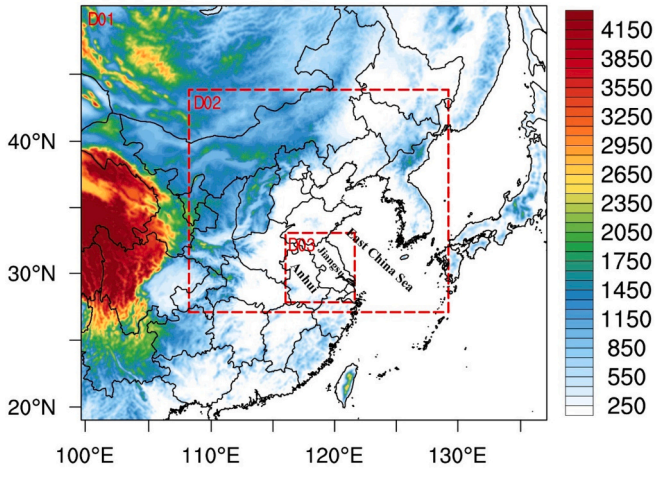

Fig. 6. Three nested modeling domains D01, D02, and D03 at 9-, 3- and 1-km resolutions with terrain elevations (m AMSL) in colour. Provinces of Anhui and Jiangsu and East China Sea are labeled in black.

within the boundary layer. Radiation processes were calculated using the Shortwave and Longwave Rapid Radiative Transfer Model (Iacono et al., 2008). The Noah land surface model (Ek et al., 2003) was utilized to calculate soil moisture and temperature, as well as the energy flux and water flux terms of the surface energy budget and water balance. To investigate the skill of bulk microphysics schemes in predicting SLW within cloud-resolving model, three sensitivity experiments were conducted using the WDM6 (Lim and Hong, 2010), NSSL (Mansell et al., 2010) and MY (Milbrandt and Yau, 2005) schemes. These three microphysics schemes were specifically chosen as they all predict two moments (i.e., mixing ratio and total number concentration) of cloud water, which are supposed to generate more accurate cloud droplet spectra than other single-moment microphysics schemes as indicated in previous studies (e.g., Labriola et al., 2019; Luo et al., 2018, Luo et al., 2021).

4. Evaluation metrics for cloud-top properties and supercooled cloud water

4.1. Cloud-top height and cloud-top temperature

The observed cloud-top height (CTH) and cloud-top temperature (CTT) are derived from the NJIAS HCFD dataset (Zhuge et al., 2024), which calculates CTT and CTH based on the architecture of the Advanced Baseline Imager (ABI) Cloud Height Algorithm (ACHA; Heidinger and Straka, 2013). Validations against the Cloud-Aerosol Lidar with Orthogonal Polarization (CALIOP) and Moderate Resolution Imaging Spectroradiometer (MODIS) MYD06 product demonstrate that the NJIAS HCFD CTT and CTH exhibit consistent accuracy across day and night. For simulations, cloud top is defined as the level of unit optical depth within the cloud (Yang et al., 2022). This is calculated at the vertical level where the integration of the layer absorption coefficients of cloud ice, cloud water and water vapor along the downward path from the model top meets a specified threshold. Vertical columns with values below this threshold are treated as cloud-free regions. The simulated CTT and CTH are determined by interpolating temperature

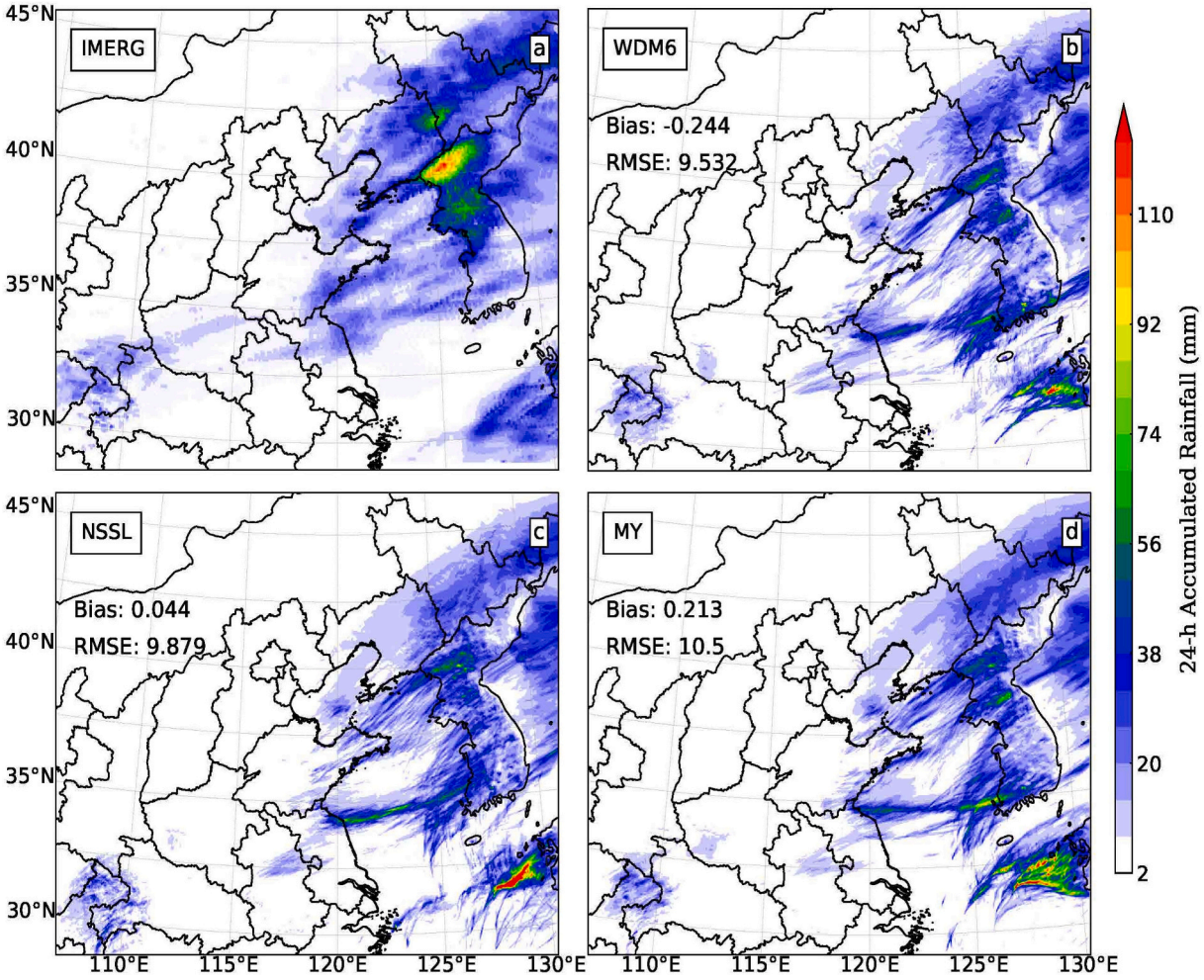

Fig. 7. Twenty-four hour accumulated precipitation (shaded, mm) between 0000 and 2400 UTC on November 122,022 from (a) the precipitation product of IMERG-F, and (b-d) precipitation of simulations utilizing WDM6, NSSL and MY schemes, respectively. Note that the corresponding Bias and RMSE are labeled in black on each panel.

and height to the cloud top levels.

4.2. Cloud top phase

The NJIAS HCFD cloud-top phase (CTP) is defined as the thermodynamic phase of the uppermost cloud layer and used for subsequent model evaluations. The cloud-top phase algorithm, developed based on Zhuge et al. (2021), categorizes cloud tops into four phases: warm water, supercooled water, ice, mixed or uncertain. This classification is achieved by employing infrared (IR) window and IR water vapor channels, along with several spectral and spatial tests. Cloud pixels with CTT above 0 °C (below 0 °C) is classified as warm (supercooled) water, while those with CTT below −30 °C are classified as ice. For CTT values between −30 and 0 °C, the cloud-top phase could be supercooled water or mixed phases. We note that as cloud-top grids with mixed or uncertain phase are in few numbers compared with other cloud-top phases and those grids are not confidently-clear classified, the mixed or uncertain phase cloud tops are not applied in the model evaluation. Moreover, for better comparison, simulated cloud-top phase is also categorized into warm water, supercooled water, and ice categories, based on the modeled mixing ratios of hydrometeors and air temperature, by

$$CTP = \begin{cases} warm\ water if\ Q_{liq} > 0\ g\ kg^{-1}, T > 0^{\circ}C \\ supercooled\ water\ if\ Q_{liq} > 0\ g\ kg^{-1}, T < 0^{\circ}C \\ Ice\ if\ Q_{frozen} > 0\ g\ kg^{-1}, Q_{liq} = 0\ g\ kg^{-1}, T < 0^{\circ}C \end{cases} \quad (1)$$

where Q_{frozen} represents the total mixing ratio of frozen hydrometeors (i.e., ice, snow, graupel, hail), Q_{liq} denotes the total mixing ratio of liquid water (i.e., cloud water and rain water) within the cloud-top layer. T is the air temperature in degree Celsius. The warm water (supercooled) water cloud-top is classified as the cloud top with Q_{liq} greater than zero and the temperature above (below) $0^{\circ}C$. When Q_{frozen} is greater than zero and Q_{liq} is zero at the cloud top layer, with temperature below $0^{\circ}C$, it is classified as ice phase.

4.3. Effective diameter of supercooled cloud water

Effective diameter (ED) is commonly used to represent the mean size of SCW droplets and it significantly influences the collection efficiency of SCW by aircraft, thereby affecting the icing rate and the morphology of ice accretion. Specifically, SCW droplets with larger ER are more likely to collide with the aircraft surface, resulting in higher droplet collection efficiency in local icing regions (e.g., Cober and Isaac, 2012; Yamazaki et al., 2021; Rocco et al., 2021). Based on the FCDP observations during this aircraft icing event, the observed effective diameter (ED_{OBS}) can be calculated by

$$ED_{OBS} = \frac{\sum n_i \times D_i^3}{\sum n_i \times D_i^2} \quad (2)$$

where n_i represents the droplet number concentration within the i_{th}

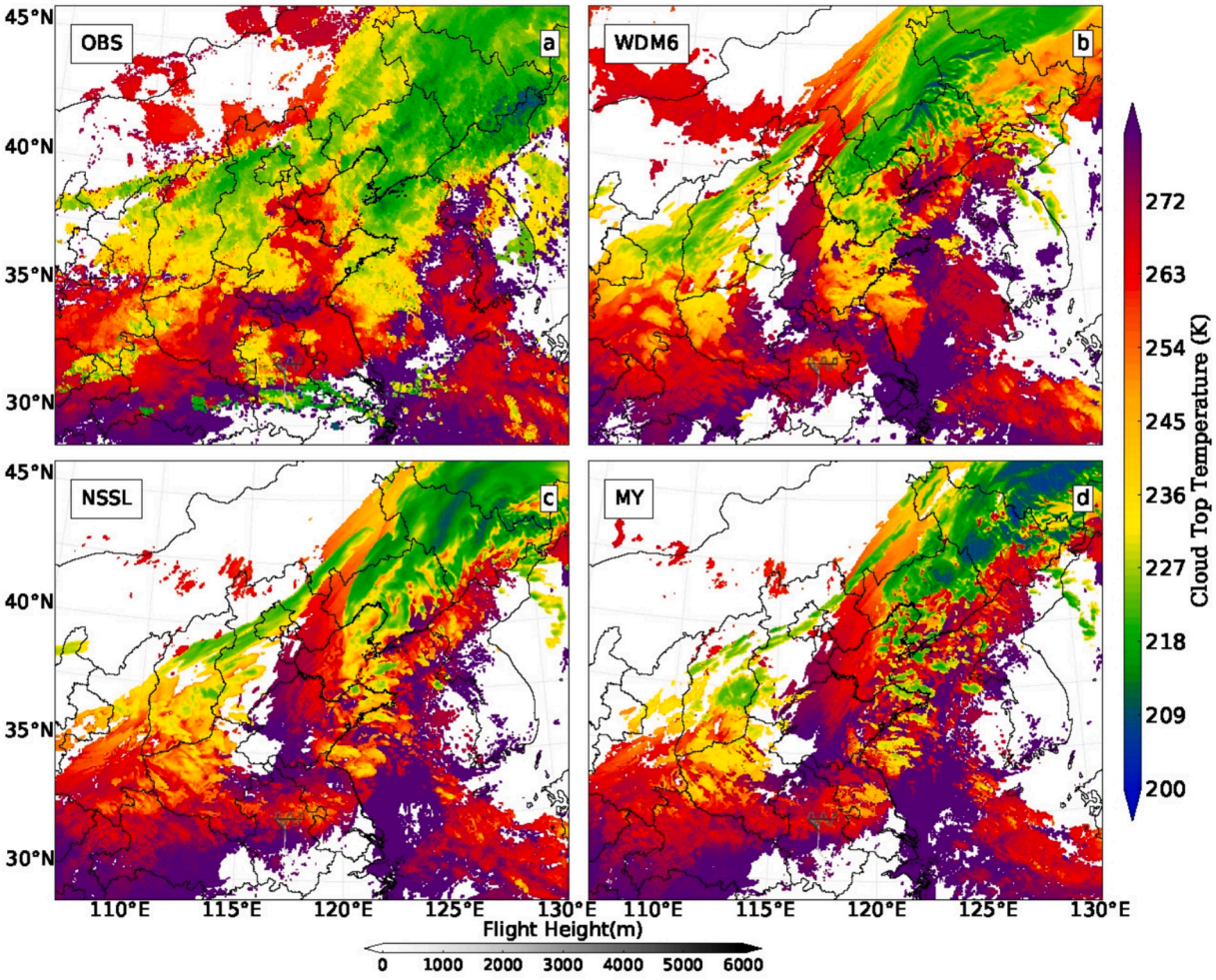

Fig. 8. Cloud top temperature (CTT, shaded, K) from (a) the Himawari-8/9 Typhoon Cloud Feature Dataset (OBS), and (b-d) CTT from the simulations utilizing WDM6, NSSL and MY schemes, respectively, at 0300 UTC on November 12, 2022. At this time, the aircraft was situated at an altitude of approximately 4300 m above the southern region of Anhui Province. Note that the gray solid lines in each panel depict the flight path and altitude during the icing event.

standard bin of the FCDP measurement, and r_i is the mean radius of the i_{th} bin.

Furthermore, to calculate the effective diameter of supercooled cloud water (SCW) from the simulations using different schemes, the cloud droplet size distribution needs to be calculated first. For the WDM6 scheme (Lim and Hong, 2010), the cloud water size distributions are calculated following the normalized form and expressed as

$$N_c(D) = Nt_c \frac{\alpha_c}{\Gamma(\upsilon_c)} \lambda_c^{\alpha_c \times \upsilon_c} D_c^{\alpha_c \times (\upsilon_c - 1)} e^{\left[-(\lambda_c \times D_c)^{\alpha_c}\right]} \tag{3}$$

Where λ_c denotes the corresponding slope parameter, while υ_c and α_c represent two dispersion parameters for the cloud water size distribution, with values set at 1 and 3, respectively. Nt_c and D_c represent the predicted total number concentration and diameter of cloud water droplets. The slope parameter λ_c can be determined by

$$\lambda_c = \left[\frac{\pi}{6}\rho_w \frac{\Gamma(\upsilon_c + 3/\alpha_c)}{\Gamma(\upsilon_c)} \frac{Nt_c}{\rho_a \times q_c}\right]^{1/3} \tag{4}$$

Where ρ_w (=1000 kg m^{-3}) represents the cloud water density, and ρ_a represents the air density, given by

$$\rho_a = {Pre}/{R_d \times T} \tag{5}$$

Where *Pre* and T represent the atmosphere pressure (in Pa) and temperature (in K), respectively, while R_d (=287.04 J kg^{-1} K^{-1}) is the dry air gas constant. For the NSSL scheme (Mansell et al., 2010), the cloud droplet size distribution is defined as:

$$N_c(D) = 3A \frac{D^{\alpha}}{\overline{D}^{\alpha+1}} e^{-B\left(\frac{D}{\overline{D}}\right)^{3\mu}} \tag{6}$$

Where D is cloud droplet diameter, parameters α, μ, and ν are set as constants with values of 2, 1, and 0, respectively.

$$A = \frac{\mu N t_c}{\Gamma\left(\frac{\nu+1}{\mu}\right)} B^{(\nu+1)/\mu} \tag{7}$$

$$B = \left[\frac{\Gamma\left(\frac{\nu+1}{\mu}\right)}{\Gamma\left(\frac{\nu+2}{\mu}\right)}\right]^{-\mu} \tag{8}$$

Eq. (6) can also be calculated based on

$$N_c(D) = N0_c e^{-\lambda_c D} \tag{9}$$

Where λ_c and $N0_c$ are the slope and intercept parameters, respectively, given by

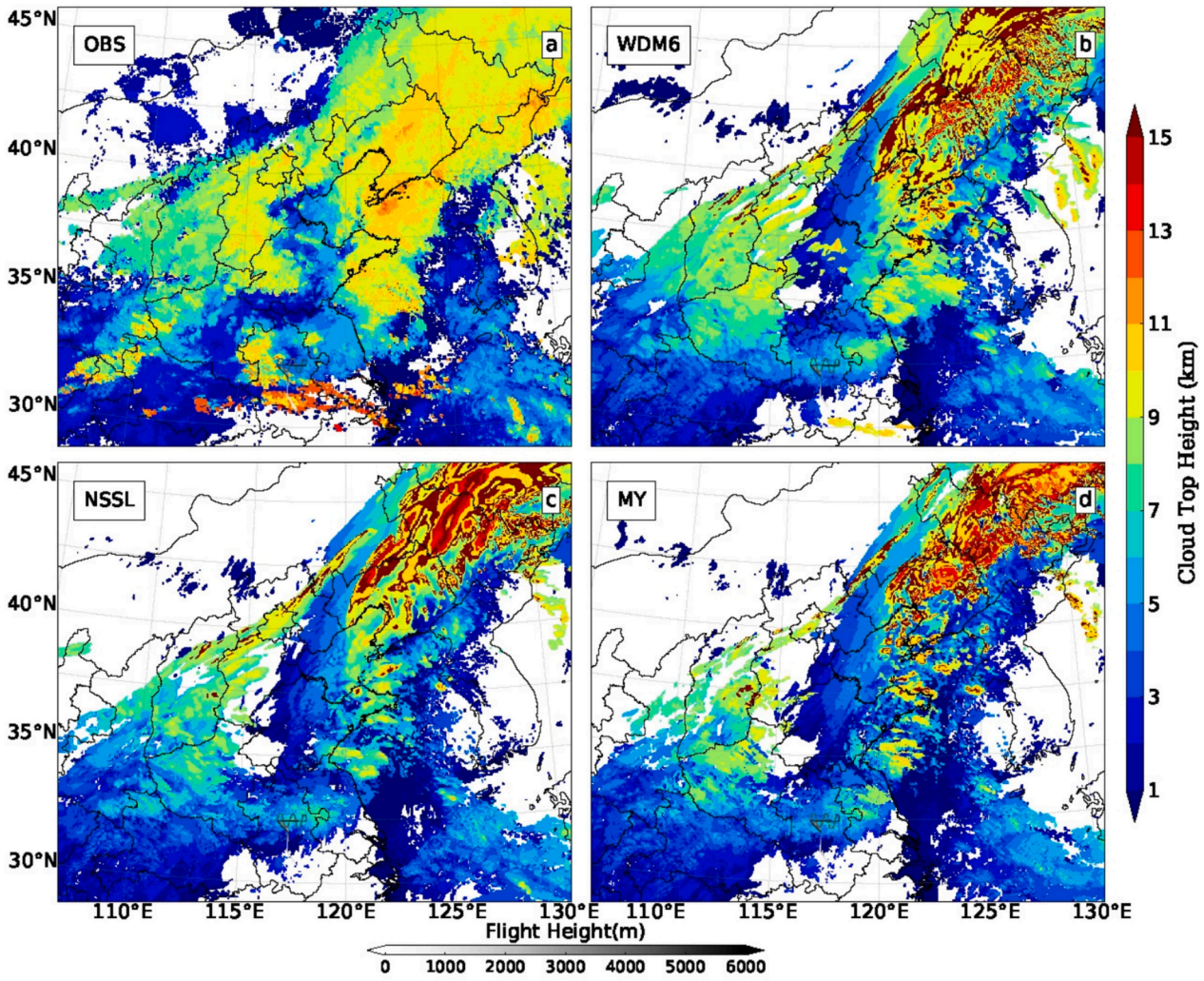

Fig. 9. Similar as in Fig. 8, but for the cloud top height (CTH, shaded, km) at 0300 UTC on November 122,022.

$$\lambda_c = \left[\frac{\pi}{6}\rho_w \frac{\Gamma(\mu+\nu)}{\Gamma(\mu)} \frac{Nt_c}{\rho_a \times q_c}\right]^{1/3} \tag{10}$$

$$N0_c = \frac{Nt_c \times \lambda_c}{\Gamma(\mu)} \tag{11}$$

For the MY scheme (Milbrandt and Yau, 2005), the cloud droplet size distribution is calculated by

$$N_c(D) = N0_c D^{\alpha_c} e^{-\lambda_c D} \tag{12}$$

Where $\alpha_c(=0)$ is the shape parameter, λ_c and $N0_c$ are the slope and intercept parameters, respectively, given by

$$\lambda_c = \left[\frac{\Gamma(1+d_c+\alpha_c)}{\Gamma(1+\alpha_c)} \frac{c_c Nt_c}{\rho_a \times q_c}\right]^{1/d_c} \tag{13}$$

$$N0_c = \frac{Nt_c \times \lambda_c^{1+\alpha_c}}{\Gamma(1+\alpha_c)} \tag{14}$$

Where $c_c = \frac{\pi}{6}\rho_w$ and d_c=3 are constants. Subsequently, the effective diameter of SCW derived from the simulations is calculated based on the calculated size distribution of cloud droplet above freezing level (Kim et al., 2003), by

$$ED_{forecast} = \frac{\int_0^\infty D^3 \times N_c(D)dD}{\int_0^\infty D^2 \times N_c(D)dD} \tag{15}$$

5. Results

5.1. Microphysical properties by airborne In-situ measurements

On that day, the aircraft conducted cloud penetration observation over central Anhui Province, equipped with a comprehensive suite of instruments. Fig. 2 presents the three-dimensional flight path colored with observed ambient temperature during the in-situ observation. The airborne in-situ measurements were executed between 0154 and 0435 UTC over central Anhui Province, providing detailed cloud microphysical observations. Instrumentation aboard the AIMMS-20 recorded three distinct climbs, reaching a maximum altitude of 4300 m at 0237 UTC and maintaining the altitude until 0325 UTC. During the subsequent 34-min, the aircraft changed its altitude to 5000 m by 0359 UTC (Figs. 3a-b). During the cruise phase (0237–0359 UTC), ambient temperature ranged between 0 and − 4 °C, with relative humidity approaching 95 % (Figs. 3c-d). Such thermodynamic conditions within cold-front systems are conducive to SCW formation and aircraft icing. Meanwhile, there exhibited significant variability in the vertical wind speeds within the frontal clouds (Fig. 3e). After 0410 UTC, the aircraft began to descend for return.

Droplet properties observed by FCDP and concurrent Ka-band radar

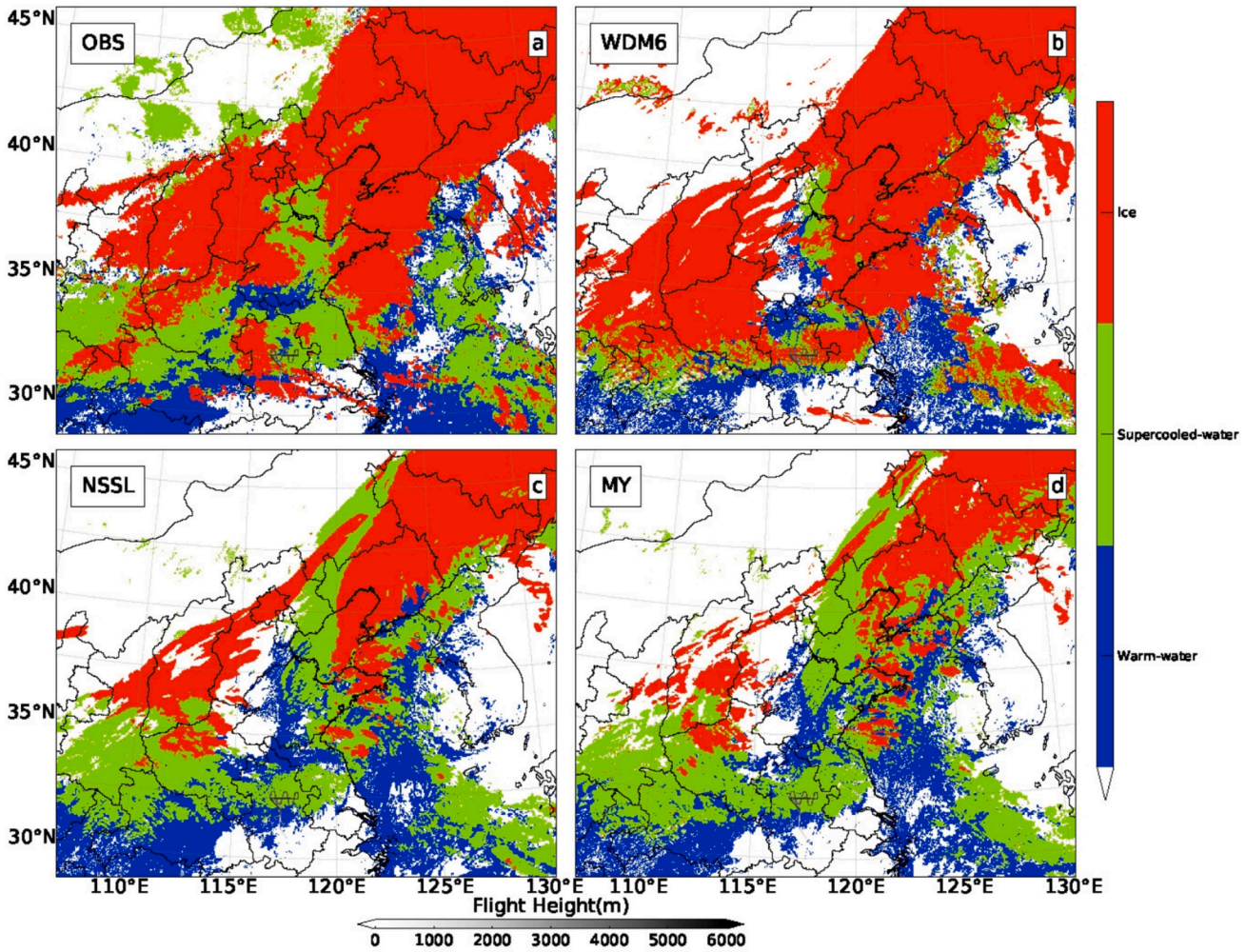

Fig. 10. Similar as in Fig. 8, but for the cloud top thermodynamic phase (shaded) at 0300 UTC on November 122,022. Three cloud-top thermodynamic phases are assigned, including the warm-water in blue, supercooled-water in green, and ice phase in red. (For interpretation of the references to colour in this figure legend, the reader is referred to the web version of this article.)

reflectivity measurements during the key flight phases are presented in Figs. 4 and 5. During the second ascending phase, the aircraft traversed warm cloud layers shortly, around only one minute (0234 to 0235 UTC). Despite the short duration, FCDP caught a high concentration of small cloud droplets (Figs. 4b, d), coinciding with radar reflectivity exceeding 20 dBZ (Fig. 5a). The subsequent cruise phase between 0307 and 0330 UTC, the aircraft encountered significant amount of SCW (~1500 cm^{-3}, $ER \sim 17\ \mu m$), with LWC reaching 1.2 g m^{-3} (Figs. 4b, c). However, radar reflectivity remained below 10 dBZ during this period (Fig. 5b), indicating that radar had limited sensitivity to small SCW droplets. However, significant aircraft icing likely occurred and it is speculated that this prompted the aircraft to climb to 5000 m to leave the intense icing layer. Previous studies have also emphasized the challenges associated with radar detection in icing conditions and the importance of risk avoidance strategies (e.g., Serke et al., 2022; Kim et al., 2024b). As indicated by high cloud radar reflectivity (>20 dBZ) in Fig. 5c, the aircraft re-entered deep stratocumulus clouds at 5000 m between 0348 and 0355 UTC, with the cloud top extending to ~6 km AGL. FCDP observations showed that the aircraft encountered numerous SCW, with *ER* exceeding 40 μm. The icing risk was enhanced within deep stratocumulus clouds, where SCW ($ER > 40\ \mu m$) also contributed to high radar reflectivity.

5.2. Model validation against satellite and airborne in-situ observations

To achieve accurate representation of SCW within clouds, precise characterization of cloud microphysical properties is essential. Sensitivity simulations using various commonly used MP schemes, including WDM6, NSSL and MY schemes are conducted at 1-km resolution, and the detailed model configurations are present in section 3. Fig. 6 shows the three-nested model domains, with the inner domain covering the Anhui and Jiangsu Provinces over Eastern China. Herein, we evaluate the model's sensitivity simulation through three critical metrics: cloud top temperature (CTT), cloud top height (CTH), and cloud top phase area (CTA), with validations against the NJIAS HCFD satellite datasets. The surface precipitation accumulated during the primary lifespan of the cold front was also verified using the IMERG-F satellite estimates across multiple simulations.

5.2.1. Surface accumulated precipitation

Fig. 7 presents the 24-h accumulated precipitation for the 3-km domain on November 12 from simulations using various MP schemes and IMERG-F observations. All simulations generally capture the observed northeast-southwest oriented rainfall band extending from northeastern of China to the eastern coastline. Note that the WDM6 scheme underestimates the accumulated rainfall, with a negative Bias of −0.244 mm and RMSE of 9.532 mm, particularly over the northern Korean Peninsula where modeled maxima (70 mm) fall below

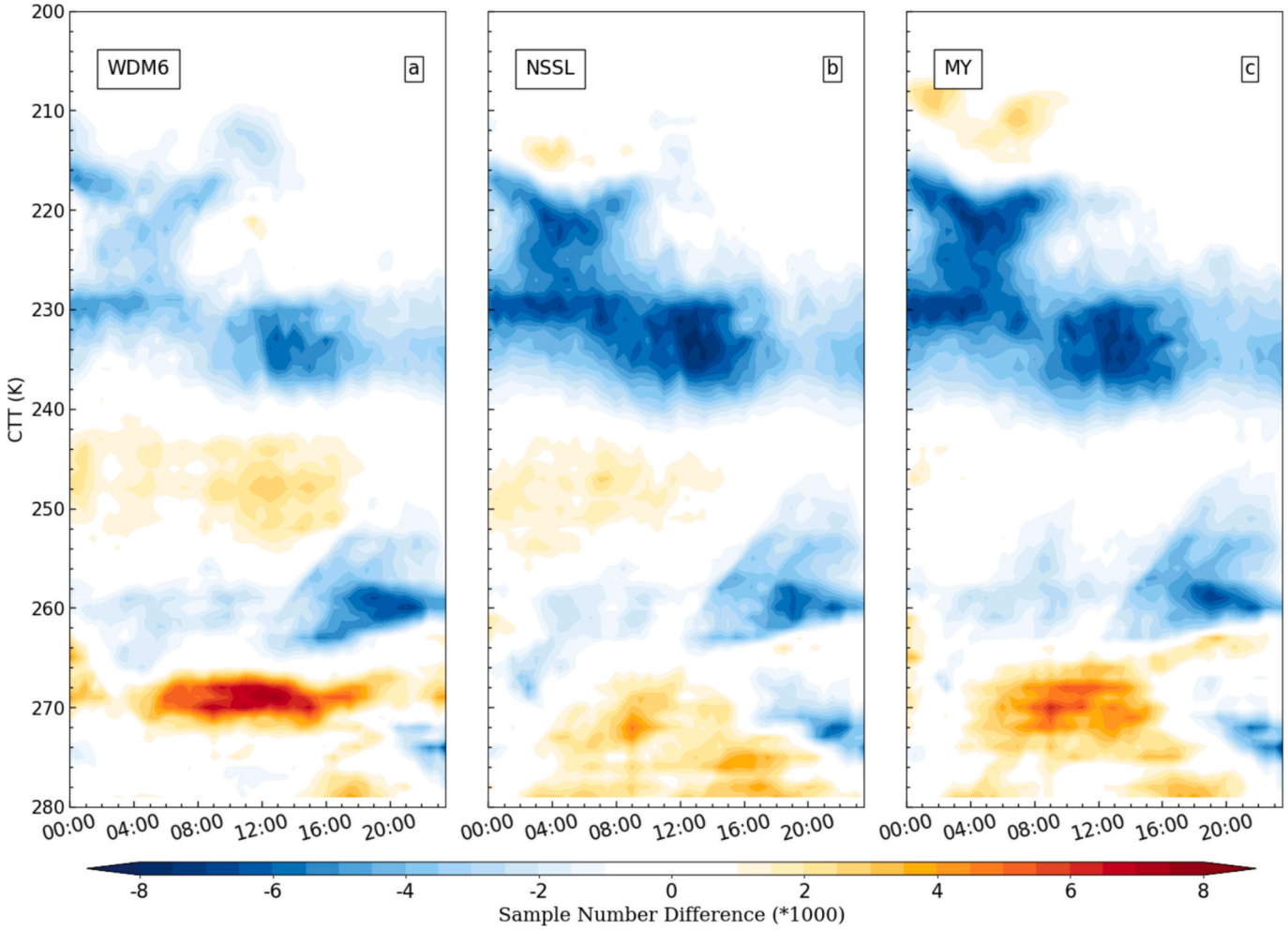

Fig. 11. Distribution of cloud top temperature (CTT, K) sampled number differences between observations and various simulations (simulations - OBS) utilizing (a) WDM6, (b) NSSL and (c) MY schemes, respectively, during 0000 and 2400 UTC November 12, 2022. A higher CTT value signifies the cloud top is positioned closer to the surface, whereas a lower value indicates the cloud top is located at a higher altitude.

observations (110 mm) (Fig. 7b). NSSL and MY schemes overestimate the rainfall slightly, with positive Bias of 0.044 and 0.213, respectively (Figs. 7c, d). The bias appears related to the rainfall centers over the East China Sea, while continental rainfall amounts remain well-reproduced. All simulations produce ~20 mm rainfall accumulation over northern Jiangsu and Anhui Provinces, matching observational records. Notably, the rainfall discrepancies over the north of Korean Peninsula suggest limitations in representing orographic enhancement processes, which may be traced to differences in the cross-mountain moisture-flux convergence over the windward slope (Tierney and Durran, 2024a, 2024b). These findings highlight the critical need for calibrating orographic precipitation of bulk MP schemes applied to East Asian cold-front systems.

5.2.2. Cloud-top temperature, height and phase

This subsection evaluates simulated cloud-top features from various MP schemes against satellite observations for the primarily frontal system. Figs. 8, 9 and 10 display the observed and simulated cloud-top temperature (CTT), height (CTH) and thermodynamic phase at 0300 UTC on November 122,022, corresponding to the aircraft's 4300 m altitude transit over southern Anhui Province. The flight path and altitude has also been indicated by the gray solid lines in each panel.

In general, the simulated cloud-top features are reproduced by the simulations, with the cold ($\langle 220K$) ice-phase cloud tops over northeastern China and warm (>260 K) liquid cloud tops prevailing in southern frontal sectors. However, the observed area of cold ice-dominated cloud top over northeastern China with CTT below 230 K and CTH above 8 km is clearly larger than all the simulations (Figs. 8, 9, 10). We also note that simulations, especially for the NSSL and MY schemes, consistently underestimate (overestimate) CTT (CTH) for the convective regions over the northeastern part of the frontal system, even producing extreme CTH values exceeding 15 km (Figs. 8–9, b-d). Similarly, Cintineo et al. (2014) and Yang et al. (2022) reported comparable biases in upper-level clouds for MY and Morrison schemes. Moreover, along the aircraft flight path over the central Anhui province, the observed cloud tops were dominated by supercooled-water, with CTT (CTH) of approximately 265 K (4-5 km) (Figs. 8-10a). However, the WDM6 scheme produces primary ice cloud tops there, with CTT and CTH of approximately 15 K colder and 1-2 km higher than the observations, respectively (Figs. 8-10b). The bias aligns with previously studies (Guo et al., 2019; Lei et al., 2020; Wang et al., 2022b), which was ascribed to its inappropriate calculations of cloud condensation nuclei activation and cloud evaporation processes. We note that the CTT and CTH simulated by the MY scheme along the flight path (~260-265 K) exhibit better agreement with the observation (Figs. 8-9c, d).

Figs. 11 and 12 presents the time series of differences in the CTT sampled number distribution and horizontal averaged CTH between the satellite observations and simulations during 0000 and 2400 UTC November 122,022. Specifically, quantitative validations of cloud top variables for SCW during this period, including biases, root-mean-

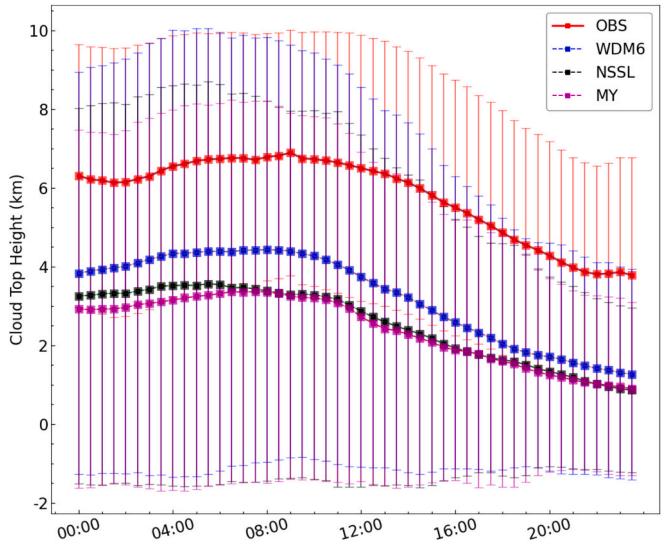

Fig. 12. Time series of cloud top height (CTH, km) during 0000 and 2400 UTC November 12, 2022 for the observations (in red) and various simulations using WDM6 (in blue), NSSL (in black) and MY (in magenta) schemes. The lines and error bars represent the mean and the standard error of observed and simulated CTH, respectively. (For interpretation of the references to colour in this figure legend, the reader is referred to the web version of this article.)

Table 1
Quantitative validations of CTT, CTH and CTA for SCW cloud tops between 0000 and 2400 UTC on November 122,022.

Name	Bias	RMSE	Correlation	Bias	RMSE	Correlation
	CTT (K) (p-value <0.0001)			CTH (km) (p-value <0.0001)		
WDM6	5.67	5.74	0.56	−0.31	0.42	0.81
NSSL	−0.91	1.62	0.36	0.49	0.55	0.80
MY	−0.67	1.56	0.55	0.46	0.51	0.79
			CTA (km^2) (p-value <0.0001)			
WDM6			−0.49	0.52	0.19	
NSSL			−0.03	0.25	0.37	
MY			0.05	0.27	0.37	

squared errors (RMSE), and correlation coefficients are summarized in Table 1. Results indicate that consistent with the cold CTT cloud fraction underestimations over northeastern China identified in Fig. 8, all simulations produce significantly less cloud pixels with CTT ranging between 240 and 220 K throughout the 24-h period (Fig. 11). The modeled averaged CTH are also underestimated of around 3 km than the observations correspondingly (Fig. 12). Specially, the WDM6 scheme predicts higher SCW cloud tops compared with the observations, with biases of CTT and CTH reaching 5.67 K and − 0.31 km, respectively. In contrast, the NSSL and MY schemes exhibit slight negative CTT biases (−0.91 K and − 0.67 K, respectively) and positive CTH biases (both below 0.5 km). These findings indicate that both schemes predict slightly higher supercooled-water cloud tops compared with observations. Specifically, the MY scheme exhibits correlation coefficients of CTT and CTH ranging from 0.55 to 0.79 (with p-values <0.0001), exhibiting better agreement with observations than other schemes.

5.3. Explicit supercooled cloud water prediction skills of MP schemes

Given that droplet size distribution and LWC of SCW can affect the height of icing angle and thickness of ice layer (Cao et al., 2018; Zeng et al., 2022), we further investigate the prediction skills of various MP schemes for explicit SCW. Fig. 13 compares the LWC, total number concentration (*Nt*) and effective diameter (*ED*) of SCW from sensitivity simulations using WDM6, NSSL and MY schemes. To verify against aircraft in-situ measurements, the simulated SCW variables were interpolated to the flight altitude of 4300 m above ground level (AGL) at 0300 UTC. The boxplots of the corresponding variables are also constructed for statistical validations between aircraft in-situ observations and simulations (Fig. 14). Note that to align the spatial resolution of the aircraft observation and simulations, the FCDP datasets are averaged over 10-s intervals assuming the aircraft airspeed was approximately 100 m s^{-1} (corresponding to about 1 km). Moreover, the particle size distributions (PSDs) of SLW for the aircraft flight region over the central Anhui Province (denoted by the red dashed rectangles in Fig. 13) are also investigated, as shown in Fig. 15. To ensure more robust conclusions, the PSDs of SLW are derived within a narrow altitude (with air temperature ranging from 0 to -4 °C), which aligns with aircraft in-situ observations during the cruise phase (c.f., Fig. 3c).

The LWC for SCW predicted by the WDM6 (MY) scheme exhibits median, 95th percentile and maximum values over aircraft flight region of 0.18, 0.98 and 1.74 (0.26, 0.90 and 1.52) g m^{-3}, respectively. These predicted values generally align with the observed LWC, with corresponding observed values of 0.32 (median), 0.92 (95th percentile) and 2.14 (maximum) g m^{-3} (Figs. 13a, c, 14a). In contrast, the NSSL scheme substantially underpredicts the LWC for SCW, with median, 95th percentile and maximum values of 0.12, 0.43 and 0.78 g m^{-3} (Fig. 14a).

Nt and *ED* of the SCW are critical factors for aircraft icing, as they influence collision-coalescence processes and icing rates (Bernstein et al., 2019; Tessendorf et al., 2021). For the observation, the SCW *Nt* and *ED* during the cruise phase were around 10^8–10^9 m^{-3} and 10–50 μm, respectively (c.f., Figs. 4b, d, 14b), with the median, 95th percentile and maximum values for *ED* of 11.81, 25.05 and 48.26 μm (Fig. 14c). However, the predicted particle size distributions of SCW show significant discrepancies among the schemes. For instance, the WDM6 scheme predicts the highest SCW *Nt* (~10^{11} m^{-3}) among all the schemes (Fig. 13d), while yielding a notably smaller *ED* (< 20 μm) compared to other schemes (Figs. 13g-i). The median and maximum values for SCW *Nt* (in base-10 logarithmic scale, m^{-3}) and *ED* by WDM6 scheme are 10.10 and 10.75, and 9.46 and 16.74 μm (Figs. 14b, c). The particle size distribution of SCW with air temperature ranging from 0 and -4 °C further reveals that the WDM6 scheme generates a high number concentration of small SCW particles, with *Nt* and *ED* primarily ranging between 10^9 and 10^{11} m^{-3} and 7–15 μm, respectively, in the aircraft flight region (Fig. 15a). Conversely, the NSSL scheme predicts a much lower SCW *Nt* (~10^7 m^{-3}) (Fig. 13e) and significantly overestimates the size of SLW, with *ED* exceeding 200 μm (Fig. 13h). The median, 95th percentile and maximum values for *ED* are 82.60, 150.01, and 326.12 μm (Fig. 14c). As indicated by the particle size distribution, it is found that the NSSL scheme produces 1–2 orders of magnitude fewer but significantly larger SCW particles (> 300 μm) compared to observations (Fig. 15b). Notably, both the *Nt* (~10^9 m^{-3}) and *ED* (~40–80 μm) of SCW produced by MY scheme match aircraft in-situ measurements the best among the schemes (Figs. 13f, i, 15c). Its corresponding median, 95th percentile and maximum values are 8.20, 8.44 and 8.86 for *Nt* (in base-10 logarithmic scale, m^{-3}), and 35.56, 51.14 and 132.51 μm for *ED* (Figs. 14b, c). These findings suggest that the MY scheme better captures the observed SCW particle size distribution, although there also exist some overestimations of the *ED*.

We noted that the discrepancies of explicit SCW prediction skills among the MP schemes are primarily attributed to the differences in the representations of microphysical processes for cloud droplets. For instance, in the WDM6 scheme, the activated cloud condensation nuclei (CCN) number concentration (n_a) is predicted based on the total particle count (including both total CCN and droplet number concentration) and the supersaturation S_w (Twomey, 1959; Khairoutdinov and Kogan, 2000; Lim and Hong, 2010). The initial CCN number concentration is set to a typical marine-type CCN value (10^8 m^{-3}), and the melting of cloud ice into cloud water is also explicitly calculated (Lim and Hong, 2010). The uncertainties in the cloud nuclei activation in the WDM6 scheme may lead to the overestimation of Nt_c above freezing level during the

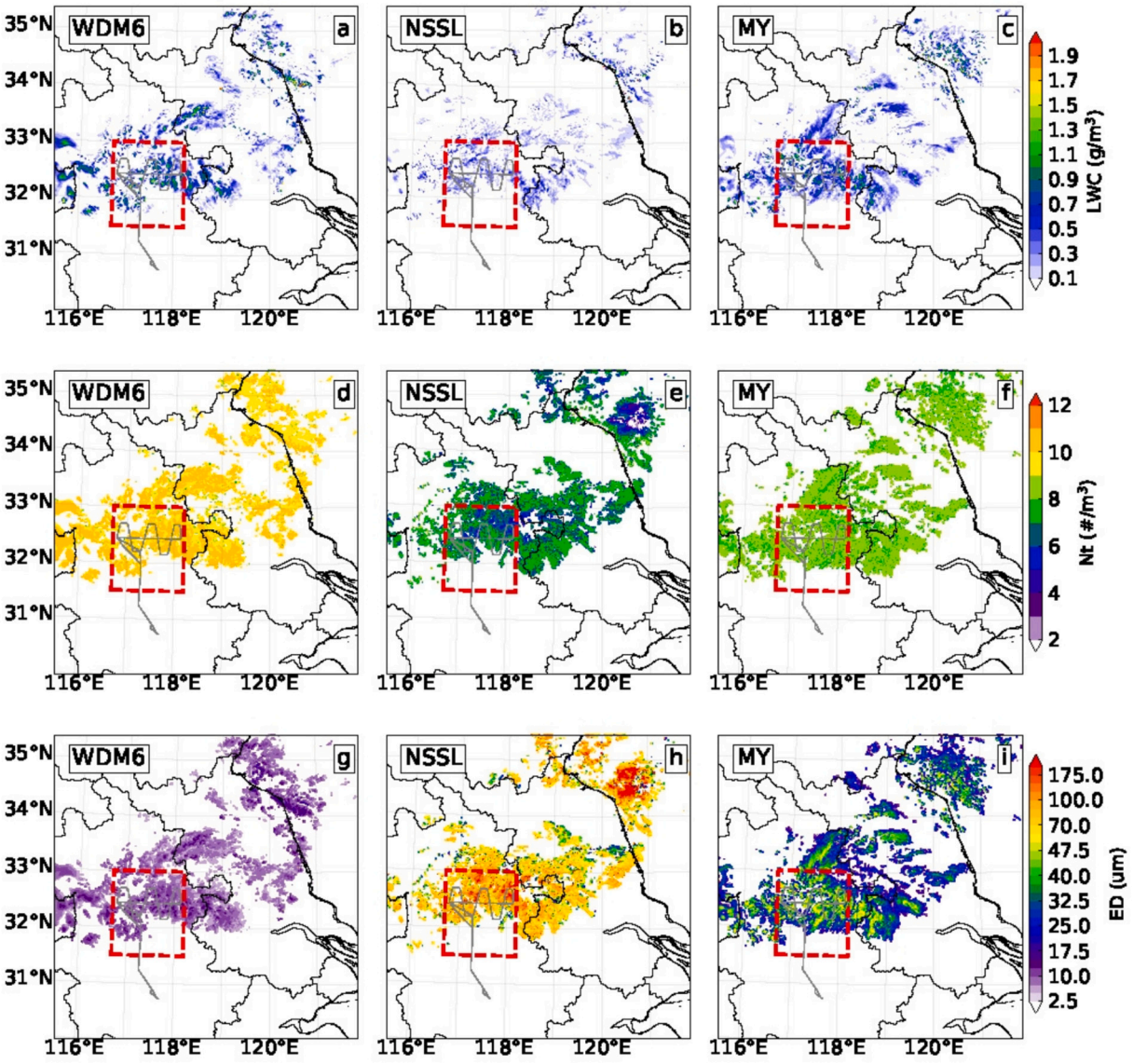

Fig. 13. Supercooled cloud water content (a-c, g m^{-3}), total number concentration (d-f, in base-10 logarithmic scale, m^{-3}), and effective diameter (g-i, μm) at an altitude of 4300 m AGL at 0300 UTC on November 122,022, for the innermost grid with a horizontal resolution of 1-km from simulations using various microphysics schemes. Specifically, panels (a, d, g), (b, e, h) and (c, f, i) correspond to simulations using the WDM6, NSSL, and MY schemes, respectively. Note that the gray solid lines in each panel depict the flight path and altitude during the icing event. The red dashed rectangle in each panel denotes the flight region, with which the simulated particle size distributions of SCW from the simulations are derived in Figs. 14 and 15. (For interpretation of the references to colour in this figure legend, the reader is referred to the web version of this article.)

icing event. Similar uncertainties have also been demonstrated in Lei et al. (2019), while it was demonstrated that the WDM6 scheme underestimated q_c and Nt_c below the melting layer. Their analysis did not extend to the PSDs or microphysical properties of SCW. Additionally, McMillen and Steenburgh (2015) noted that WDM6 scheme produced a lower cloud water mixing ratio than the Thompson scheme, likely due to its overestimation of graupel collection of cloud water in moist convection systems. However, in our study of an aircraft icing event, the clouds were predominantly stratiform, making graupel-cloud water interactions negligible.

Moreover, in the NSSL scheme, cloud droplet initiation and growth are calculated separately at the cloud base and within the cloud interior, respectively. Additionally, this scheme predicts the bulk concentration of CCN and the average bulk densities of graupel and hail (Ziegler, 1985; Mansell et al., 2010). We also noted that the uncertainties associated with warm-rain processes, particularly autoconversion and the collision-coalescence of cloud droplets are likely contributing factors to the significant underestimation (overestimation) of *Nt* (*ED*) of SCW within the NSSL scheme.

The differences in the initiation and calculation of cloud droplet freezing into ice crystals can further contribute to variations in the predicted PSD of SLW among the schemes. In the MY scheme, homogeneous freezing of cloud droplets is activated at temperatures below -30 °C, following Kong and Yau (1997). In contrast, the NSSL scheme initiates heterogeneous drop freezing through the continuous collection and capture of ice crystals, with the process depending on droplet fall speed and the fractions of crystals and drops exceeding specific minimum diameters (10 μm for crystals and 500 μm for cloud droplets). The WDM6 scheme accounts for both homogeneous and heterogeneous freezing mechanisms for cloud water conversion into ice (Lim and Hong, 2010). Above all, detailed microphysical budget analyses of the source and sink terms governing the rates of change for q_c and Nt_c are beneficial to clarify scheme-specific discrepancies in SLW predictions.

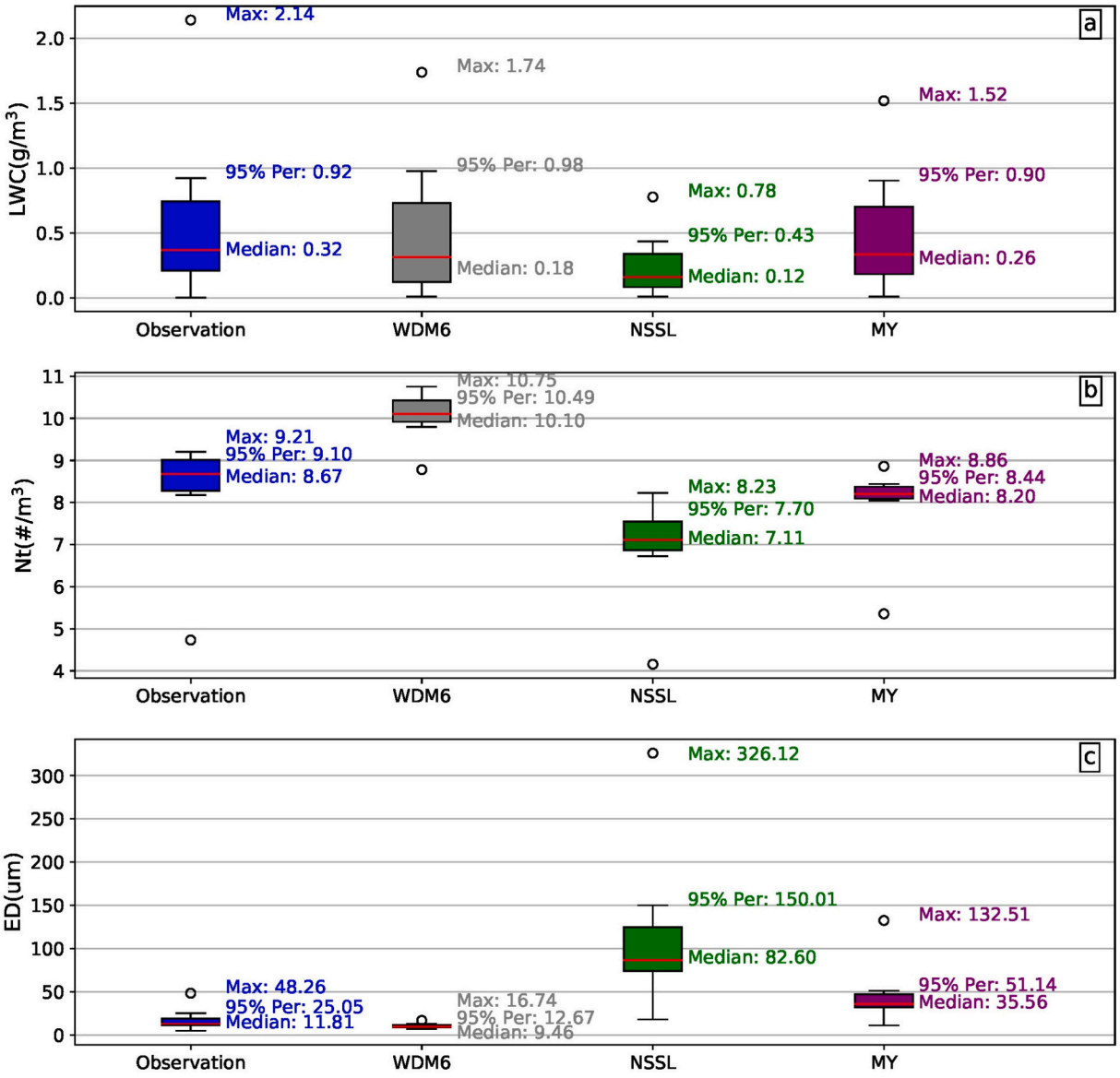

Fig. 14. Boxplots of (a) supercooled cloud water content (LWC, g m^{-3}), (b) total number concentration (Nt in base-10 logarithmic scale, m^{-3}), and (c) effective diameter (ED, μm) from in-situ aircraft observations at 4300 m AGL during the cruise phase, and corresponding interpolations from simulations using the WDM6, NSSL and MY schemes for an altitude of 4300 m AGL at 0300 UTC on November 122,022, within the red dashed rectangle in Fig. 13. The maximum values, 95th percentiles and median values are labeled beside each box in different colors for clear identification. (For interpretation of the references to colour in this figure legend, the reader is referred to the web version of this article.)

6. Summary and conclusions

This study investigates the cloud microphysical properties of an aircraft icing event over Eastern China on November 122,022, using in-situ aircraft measurements and satellite observations. Aircraft observations revealed that icing occurred at altitudes with temperature ranging from 0 and -5 °C within the frontal zone. Notably, the concentration of supercooled cloud water (SCW) reached up to 10^9 m^{-3}, with an effective diameter exceeding 45 μm and a liquid water content (LWC) of approximately 1.2 g m^{-3}.

Besides, sensitivity simulations using various commonly used two-moment bulk microphysics schemes within WRF model, i.e., WDM6, NSSL and MY schemes at 1-km horizontal resolution, are conducted for the icing event. Comparisons against satellite observations indicate that WDM6, NSSL and MY schemes generally capture the movement of the frontal system and the surface precipitation distribution. However, they consistently underestimate the presence of upper-level clouds with cloud top temperature (CTT) below 240 K, leading to significant underestimations of averaged cloud top height (CTH). Specifically, the WDM6 scheme produces ice cloud-top area (CTA) closest to satellite observations but only produces approximately half of the observed CTA for supercooled water clouds. In contrast, MY scheme demonstrates superior performance in simulating the temporal evolution of CTT (Bias: -0.67 K, RMSE: 1.56, Correlation: 0.55) and CTH (Bias: 0.19 km, RMSE: 0.23, Correlation: 0.70) for supercooled water cloud tops.

Furthermore, the explicit prediction skills of supercooled liquid water of the microphysics schemes at 1-km grid resolution have also been evaluated by compared with in-situ airborne measurements. The microphysical characteristics of LWC, *Nt* and *ED* have been examined at 4300 m AGL during the cruise phase of the flight in detail. The particle size distribution of SLW within the aircraft flight region from the simulations using various MP schemes have also been investigated. Results indicate that WDM6 scheme produces an excessive concentration of small SCW particles with an effective diameter smaller than 20 μm,

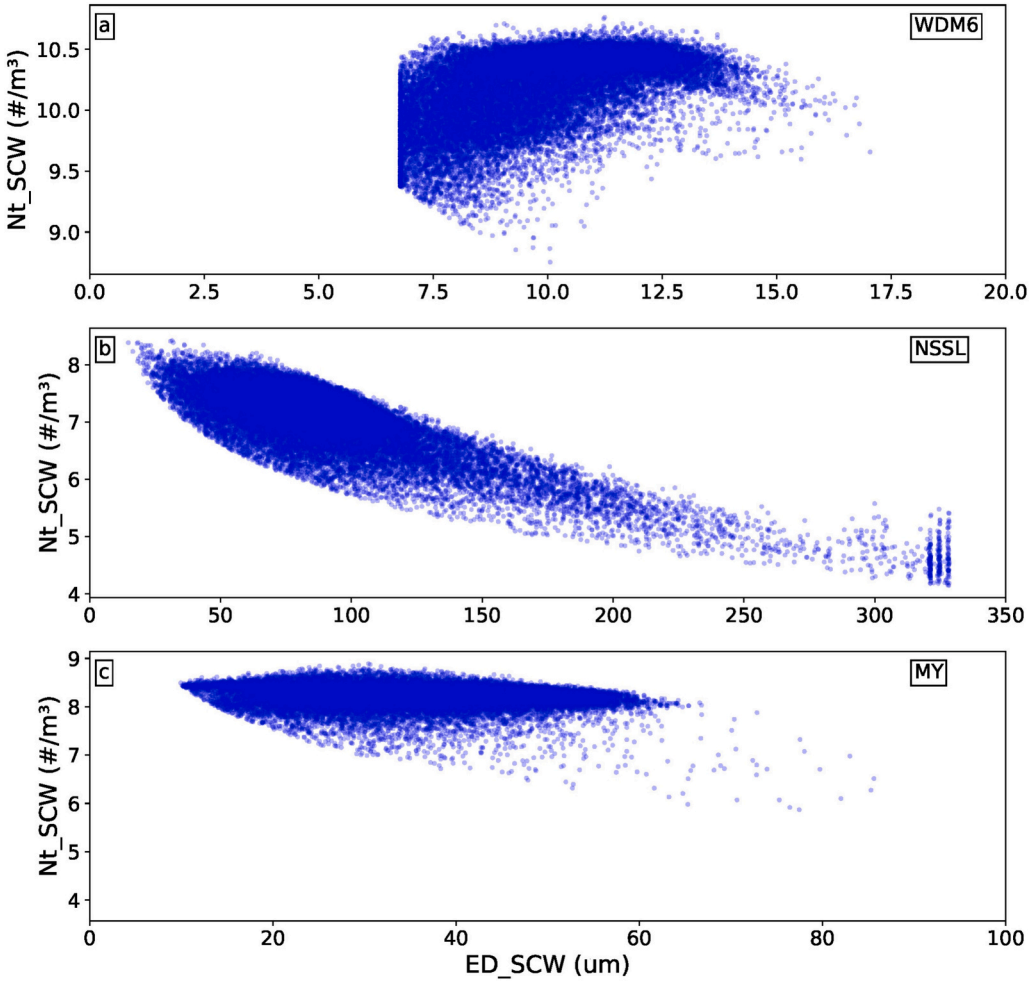

Fig. 15. Scatterplots of effective diameter (μm) and total number concentration (in base-10 logarithmic scale, m^{-3}) of supercooled cloud water (ED_SCW vs Nt_SCW) with air temperature ranging from 0 to -4 °C. The results are derived from the sensitivity simulations using various schemes for the aircraft flight region over the central Anhui Province within the red dashed rectangle in each panel of Fig. 13. (For interpretation of the references to colour in this figure legend, the reader is referred to the web version of this article.)

while NSSL scheme produces 1–2 order of magnitudes fewer but significantly overestimates the size of SCW, with *ED* exceeding 200 μm. Among the schemes, MY scheme's forecast of the SCW particle size spectrum aligned most closely with aircraft in-situ measurements.

To improve explicit prediction skills of SCW, further research should focus on validating and refining microphysical process parameterizations and critical parameters calculations associated with cloud droplet growth and particle size distributions. This work not only advances our understanding of cloud microphysical processes underlying aircraft icing events but also underscores the pivotal role of microphysical parameterizations in shaping SCW predictions. Our findings highlight the urgent need for refined microphysical parameterizations to enhance the reliability of aviation hazard forecasts and mitigate risks associated with in-flight icing—a challenge of paramount importance for global aviation safety. We acknowledge that the conclusions drawn in this study are based on a single aircraft icing case and its corresponding simulations. Given the inherent complexity of icing cloud microphysical characteristics, further investigations across diverse icing scenarios, geographic locations, and extended time periods are essential to validate and generalize our results. Additionally, comparisons between aircraft observational datasets (with a temporal resolution of 1 s along the flight path) and model simulations (with a spatial resolution of 1 km over the aircraft flight region) inherently involve uncertainties. Moreover, more detailed budget analyses in terms of SLW from different microphysics schemes would provide deeper insights into the microphysical processes governing SLW genesis, as well as the discrepancies in representing these processes across various microphysics schemes.

CRediT authorship contribution statement

Liping Luo: Writing – original draft, Visualization, Validation, Supervision, Software, Project administration, Methodology, Investigation, Funding acquisition, Formal analysis, Data curation, Conceptualization. **Ming Xue:** Writing – review & editing, Methodology, Funding acquisition, Formal analysis, Conceptualization. **Xin Xu:** Writing – review & editing, Validation, Methodology, Funding acquisition, Conceptualization. **Lin Deng:** Methodology, Investigation, Funding acquisition. **Junxia Li:** Validation, Methodology, Data curation. **Rong Zhang:** Visualization, Methodology, Investigation, Data curation.

Declaration of competing interest

The authors declare that they have no known competing financial interests or personal relationships that could have appeared to influence the work reported in this paper.

Acknowledgments

This work was primarily sponsored by the National Natural Science Foundation of China (Grant 42475200), and the Aviation Science Fund

of China (Grant 2024M074052002). This work was also funded by Shanghai Typhoon Institute, China Meteorological Administration (TFJJ202406), Open Foundation of China Meteorological Administration Hydro-Meteorology Key Laboratory (24SWQXZ010), Nanjing Joint Institute for Atmospheric Sciences (BJG202505), and Meteorological Joint Fund Project of Guangdong Province (2024A1515510010). Computational support was provided by High Performance Computing Platform of Nanjing University of Aeronautics and Astronautics. We sincerely thank the anonymous reviewers for their constructive comments, which substantially helped us improve our study. We also extend our appreciate to Hongyang Wang from Nanjing University of Aeronautics and Astronautics, for assisting with the analysis of aircraft in-situ observations.

Data availability

Simulation forcing is from ERA5.The satellite datasets can be accessed online for IMERG (Huffman et al., 2023) and NJIAS HCFD (Zhuge et al., 2024). Modeling data produced by this study as well as the verification data are available Zenodo at Luo (2025).

References

Beck, J., Coauthors, 2020. An Evaluation of a Hybrid, Terrain-Following Vertical Coordinate in the WRF-Based RAP and HRRR Models. https://doi.org/10.1175/WAF-D-19-0146.1.

Bernstein, B.C., Coauthors, 2021. The in-cloud icing and large-drop experiment science and operations plan (no. DOT/FAA/TC-21/29). In: *United States. Department of Transportation. Federal Aviation Administration.* William J. Hughes Technical Center.

Bernstein, B.C., McDonough, F., Politovich, M.K., Brown, B.G., Ratvasky, T.P., Miller, D. R., Wolff, C.A., Cunning, G., 2005. Current icing potential: Algorithm description and comparison with aircraft observations. J. Appl. Meteorol. Climatol. 44, 969–986. https://doi.org/10.1175/JAM2246.1.

Bernstein, B.C., Rasmussen, R.M., McDonough, F., Wolff, C., 2019. Keys to differentiating between small- and large-drop icing conditions in continental clouds. J. Appl. Meteorol. Climatol. 58, 1931–1953. https://doi.org/10.1175/JAMC-D-18-0038.1.

Cao, Y., Tan, W., Wu, Z., 2018. Aircraft icing: an ongoing threat to aviation safety. Aerosp. Sci. Technol. 75, 353–385. https://doi.org/10.1016/j.ast.2017.12.028.

Cintineo, R., Otkin, J.A., Xue, M., Kong, F., 2014. Evaluating the performance of planetary boundary layer and cloud microphysical parameterization schemes in convection-permitting ensemble forecasts using synthetic GOES-13 satellite observations. Mon. Weather Rev. 142, 163–182. https://doi.org/10.1175/MWR-D-13-00143.1.

CobeG, A. Isaac, Ga, S., Strapp, J.W., 1995. Aircraft icing measurements in East Coast Winter storms. J. Appl. Meteorol. Climatol. 34, 88–100. https://doi.org/10.1175/1520-0450-34.1.88.

Cober, S.G., Isaac, G.A., 2012. Characterization of aircraft icing environments with supercooled large drops for application to commercial aircraft certification. J. Appl. Meteorol. Climatol. 51, 265–284. https://doi.org/10.1175/JAMC-D-11-022.1.

Cornell, D., Donahue, C.A., Keith, C., 1995. A Comparison of Aircraft Icing Forecast Models.

Dawson, D.T., Xue, M., Milbrandt, J.A., Yau, M.K., 2010. Comparison of evaporation and cold pool development between single-moment and multimoment bulk microphysics schemes in idealized simulations of tornadic thunderstorms. Mon. Weather Rev. 138, 1152–1171. https://doi.org/10.1175/2009MWR2956.1.

Duzenli, E., Yucel, I., Pilatin, H., Yilmaz, M.T., 2021. Evaluating the performance of a WRF initial and physics ensemble over Eastern Black Sea and Mediterranean regions in Turkey. Atmos. Res. 248, 105184. https://doi.org/10.1016/j.atmosres.2020.105184.

Ek, M.B., Mitchell, K.E., Lin, Y., Rogers, E., Grunmann, P., Koren, V., Gayno, G., Tarpley, J.D., 2003. Implementation of Noah land surface model advances in the National Centers for environmental prediction operational mesoscale Eta model. J. Geophys. Res. Atmos. 108. https://doi.org/10.1029/2002JD003296.

Ellrod, G.P., Bailey, A.A., 2007. Assessment of aircraft icing potential and maximum icing altitude from geostationary meteorological satellite data. Weather Forecast. 22, 160–174. https://doi.org/10.1175/WAF984.1.

Gao, S., Yang, S., Xue, M., Cui, C., 2008. Total deformation and its role in heavy precipitation events associated with deformation-dominant flow patterns. Adv. Atmos. Sci. 25, 11–23. https://doi.org/10.1007/s00376-008-0011-y.

Grosvenor, D.P., Choularton, T.W., Lachlan-Cope, T., Gallagher, M.W., Crosier, J., Bower, K.N., Ladkin, R.S., Dorsey, J.R., 2012. In-situ aircraft observations of ice concentrations within clouds over the Antarctic Peninsula and Larsen Ice Shelf. Atmos. Chem. Phys. 12, 11275–11294. https://doi.org/10.5194/acp-12-11275-2012.

Gultepe, I., Coauthors, 2019. A review of high impact weather for aviation meteorology. Pure Appl. Geophys. 176, 1869–1921. https://doi.org/10.1007/s00024-019-02168-6.

Guo, Q., Coauthors, 2023. evaluation of different cloud microphysics schemes on the meteorological condition prediction of aircraft icing. Transact. Nanjing Univ. Aeronaut. Astronaut. 40, 124–136. https://doi.org/10.16356/j.1005-1120.2023.02.002.

Guo, J., Lei, H., Chen, Di, Yang, J., 2019. Evaluation of the WDM6 scheme in the simulation of number concentrations and drop size distributions of warm-rain hydrometeors: comparisons with the observations and other schemes. Atmos. Oceanic Sci. Lett. 12, 458–466. https://doi.org/10.1080/16742834.2019.1670584.

Heidinger, A.K., Straka, W.C., 2013. III: GOES-R Advanced Baseline Imager (ABI) Algorithm Theoretical Basis Document for Cloud Mask (Version 3.0), 104 pp. https://www.star.nesdis.noaa.gov/goesr/documents/ATBDs/Baseline/ATBD_GOES R_Cloud_Mask_v3.0_Jul2012.pdf.

Hersbach, H., Coauthors, 2020. The ERA5 global reanalysis. Q. J. R. Meteorol. Soc. 146, 1999–2049. https://doi.org/10.1002/qj.3803.

Hong, S.-Y., Noh, Y., Dudhia, J., 2006. A New Vertical Diffusion Package with an Explicit Treatment of Entrainment Processes. https://doi.org/10.1175/MWR3199.1.

Huffman, G.J., Stocker, E.F., Bolvin, D.T., Nelkin, E.J., Tan, Jackson, 2023. GPM IMERG final precipitation L3 half hourly 0.1 degree x 0.1 degree V07, Greenbelt, MD. In: Goddard Earth Sciences Data and Information Services Center (GES DISC), Accessed: [Data Access Date]. https://doi.org/10.5067/GPM/IMERG/3B-HH/07.

Iacono, M.J., Delamere, J.S., Mlawer, E.J., Shephard, M.W., Clough, S.A., Collins, W.D., 2008. Radiative forcing by long-lived greenhouse gases: Calculations with the AER radiative transfer models. J. Geophys. Res. Atmos. 113. https://doi.org/10.1029/2008JD009944.

Isaac, G., Cober, S., Korolev, A., Strapp, J., Tremblay, A., 1999. Canadian Freezing Drizzle Experiment. In: *37th Aerospace Sciences Meeting and Exhibit*, 37th Aerospace Sciences Meeting and Exhibit, Reno, NV, U.S.A. American Institute of Aeronautics and Astronautics. https://doi.org/10.2514/6.1999-492.

Isaac, G., Cober, S.G., Strapp, J.W., Korolev, A., Tremblay, A., Marcotte, D.L., 2001. Recent Canadian research on aircraft in-flight icing. Can. Aeronaut. Space J. 44, 213–222.

Jensen, A.A., Weeks, C., Xu, M., Landolt, S., Korolev, A., Wolde, M., DiVito, S., 2023. The prediction of supercooled large drops by a microphysics and a machine learning model for the ICICLE field campaign. Weather Forecast. 38, 1107–1124. https://doi.org/10.1175/WAF-D-22-0105.1.

Khairoutdinov, M., Kogan, Y., 2000. A new cloud physics parameterization in a Large-Eddy simulation model of marine stratocumulus. Mon. Weather Rev. 128, 229–243. https://doi.org/10.1175/1520-0493(2000)128<0229:ANCPPI>2.0.CO;2.

Kim, B.-G., Schwartz, S.E., Miller, M.A., Min, Q., 2003. Effective radius of cloud droplets by ground-based remote sensing: Relationship to aerosol. J. Geophys. Res. Atmos. 108. https://doi.org/10.1029/2003JD003721.

Kim, E.-T., Kim, J.-H., Kim, S.-H., Morcrette, C., 2024a. Operational aviation icing forecast algorithm for the Korea Meteorological Administration. Weather Forecast. 39, 501–521. https://doi.org/10.1175/WAF-D-23-0160.1.

Kim, Y., Ye, B.-Y., Suk, M.-K., 2024b. AIDER: Aircraft Icing potential Area DEtection in Real-Time using 3-dimensional radar and atmospheric variables. Remote Sens. 16, 1468. https://doi.org/10.3390/rs16081468.

Kong, F., Yau, M.K., 1997. An explicit approach to microphysics in MC2. Atmosphere-Ocean 35, 257–291. https://doi.org/10.1080/07055900.1997.9649594.

Labriola, J., Snook, N., Jung, Y., Xue, M., 2019. Explicit ENSEMBLE Prediction of Hail in 19 May 2013 Oklahoma City Thunderstorms and Analysis of Hail Growth Processes with several Multimoment Microphysics Schemes. https://doi.org/10.1175/MWR-D-18-0266.1.

Lei, H., Guo, J., Chen, D., Yang, J., 2019. Comparison of two double-moment microphysics schemes in aspects of warm-rain droplet spectra and raindrop budget. Atmos. Oceanic Sci. Lett. 12, 424–433. https://doi.org/10.1080/16742834.2019.1664882.

Lei, GD, J., Yangn, C.J., 2020. Systematic Bias in the prediction of warm-rain hydrometeors in the WDM6 microphysics scheme and modifications. J. Geophys. Res. Atmos. 125, e2019JD030756. https://doi.org/10.1029/2019JD030756.

Lim, K.-S.S., Hong, S.-Y., 2010. Development of an effective double-moment cloud microphysics scheme with prognostic Cloud Condensation Nuclei (CCN) for weather and climate models. Mon. Weather Rev. 138, 1587–1612. https://doi.org/10.1175/2009MWR2968.1.

Listowski, C., Delanoë, J., Kirchgaessner, A., Lachlan-Cope, T., King, J., 2019. Antarctic clouds, supercooled liquid water and mixed phase, investigated with DARDAR: geographical and seasonal variations. Atmos. Chem. Phys. 19, 6771–6808. https://doi.org/10.5194/acp-19-6771-2019.

Loftus, A.M., Cotton, W.R., Carrió, G.G., 2014. A triple-moment hail bulk microphysics scheme. Part I: Description and initial evaluation. Atmos. Res. 149, 35–57. https://doi.org/10.1016/j.atmosres.2014.05.013.

Luo, L., Xue, M., Zhu, K., Zhou, B., 2018. Explicit prediction of hail in a long-lasting multicellular convective system in Eastern China using multimoment microphysics schemes. J. Atmos. Sci. 75, 3115–3137. https://doi.org/10.1175/JAS-D-17-0302.1.

Luo, Liping, 2025. Datasets for 2025-Aircraft Icing over Eastern China [Data set]. Zenodo. https://doi.org/10.5281/zenodo.15581942.

Luo, M., Zhu, X.K., Wang, Z., 2021. Diagnosing the shape parameters of the gamma particle size distributions in a two-moment microphysics scheme and improvements to explicit hail prediction. Atmos. Res. 258, 105651. https://doi.org/10.1016/j.atmosres.2021.105651.

Ma, Z., Coauthors, 2021. Sensitivity of snowfall forecast over North China to ice crystal deposition/sublimation parameterizations in the WSM6 cloud microphysics scheme. Q. J. R. Meteorol. Soc. 147, 3349–3372. https://doi.org/10.1002/qj.4132.

Mansell, E.R., Ziegler, C.L., Bruning, E.C., 2010. Simulated electrification of a small thunderstorm with two-moment bulk microphysics. J. Atmos. Sci. 67, 171–194. https://doi.org/10.1175/2009JAS2965.1.

McMillen, J.D., Steenburgh, W.J., 2015. Impact of Microphysics Parameterizations on Simulations of the 27 October 2010 Great Salt Lake–Effect Snowstorm. https://doi.org/10.1175/WAF-D-14-00060.1.

Merino, A., Coauthors, 2019. Aircraft icing: In-cloud measurements and sensitivity to physical parameterizations. Geophys. Res. Lett. 46, 11559–11567. https://doi.org/10.1029/2019GL084424.

Milbrandt, J.A., Yau, M.K., 2005. A multimoment bulk microphysics parameterization. Part II: a proposed three-moment closure and scheme description. J. Atmos. Sci. 62, 3065–3081. https://doi.org/10.1175/JAS3535.1.

Miller, D., Ratvasky, T., Bernstein, B., McDonough, F., Strapp, J., 1998. NASA/FAA/NCAR Supercooled large droplet icing flight research: Summary of winter 96-97 flight operations. *NASA/TM-1998-206620, AIAA-98-0577*.

Rasmussen, R., Coauthors, 1992. Winter Icing and Storms Project (WISP). Bull. Am. Meteorol. Soc. 73, 951–976. https://doi.org/10.1175/1520-0477(1992)073<0951:WIASP>2.0.CO;2.

Reveley, M.S., Withrow, C.A., Barr, L.C., Evans, J.K., Leone, K.M., Jones, S.M., 2014. *Aviation Trends Related to Atmospheric Environment Safety Technologies Project Technical* Challenges. accessed 28 October 2025. https://ntrs.nasa.gov/citations/20140013257.

Rocco, E.T., Han, Y., Kreeger, R., Palacios, J., 2021. Super-cooled large droplet experimental reproduction, ice shape modeling, and scaling method assessment. AIAA J. 59, 1277–1295. https://doi.org/10.2514/1.J059401.

Schultz, P., Politovich, M.K., 1992. Toward the improvement of aircraft-icing forecasts for the continental United States. Weather Forecast. 7, 491–500. https://doi.org/10.1175/1520-0434(1992)007<0491:TTIOAI>2.0.CO;2.

Serke, D.J., Ellis, S.M., Tessendorf, S.A., Albo, D.E., Hubbert, J.C., Haggerty, J.A., 2022. Radar Icing Algorithm: Algorithm Description and Comparison with Aircraft Observations. https://doi.org/10.1175/JTECH-D-21-0003.1.

Skamarock, W.C., Coauthors, 2019. A Description of the Advanced Research WRF Model Version 4.

Stewart, R.E., 1991. Canadian Atlantic Storms Program: Progress and plans of the meteorological component. Bull. Am. Meteorol. Soc. 72, 364–371. https://doi.org/10.1175/1520-0477(1991)072<0364:CASPPA>2.0.CO;2.

Sun, J., Cai, M., Wang, F., Shi, Y., 2019. A case study of aircraft icing conditions in Anqing Area. Meteorol. Monthly 45, 1341–1351 (in Chinese).

Tessendorf, S.A., Coauthors, 2021. Differentiating freezing drizzle and freezing rain in HRRR model forecasts. Weather Forecast. 36, 1237–1251. https://doi.org/10.1175/WAF-D-20-0138.1.

Thompson, G., Bruintjes, R.T., Brown, B.G., Hage, F., 1997. Intercomparison of in-flight icing algorithms. Part I: WISP94 real-time icing prediction and evaluation program. Weather Forecast. 12, 878–889. https://doi.org/10.1175/1520-0434(1997)012<0878:IOIFIA>2.0.CO;2.

Thompson, G., Politovich, M.K., Rasmussen, R.M., 2017. A numerical weather model's ability to predict characteristics of aircraft icing environments. Weather Forecast. 32, 207–221. https://doi.org/10.1175/WAF-D-16-0125.1.

Tierney, Durran, D., 2024b. Underestimates of Orographic Precipitation in Idealized Simulations. Part II: Underlying Causes. https://doi.org/10.1175/JAS-D-23-0176.1.

Tierney, L., Durran, D., 2024a. Underestimates of Orographic Precipitation in Idealized Simulations. Part I: Evidence from Unidirectional Warm-Sector Environments. https://doi.org/10.1175/JAS-D-23-0177.1.

Twomey, S., 1959. The nuclei of natural cloud formation: the supersaturation in natural clouds and the variation of cloud droplet concentrations. Pure Appl. Geophys. 43, 243–249.

Wang, T., Zhu, J., Lei, H., Shi, Y., Guo, J., Gao, Z., 2022b. Comparison of microphysics parameterization schemes on cloud macrophysics forecasts for mixed convective-stratiform cloud events. Atmos. Res. 277, 106284. https://doi.org/10.1016/j.atmosres.2022.106284.

Wang, Y., 2023. Analysis of rainstorm process in South China from September 7 to 8, 2022. J. Geosci. Environ. Protect. 11, 161–167. https://doi.org/10.4236/gep.2023.118009.

Wang, Z., Zhou, X., Wu, J., Li, B., Lin, Y., Yan, W., Zhang, Y., 2022a. Weather conditions and cloud microphysical characteristics of an aircraft severe icing process. J. Appl. Meteorol. Sci. 33, 555–567 (in Chinese).

Wei, P., Coauthors, 2023. On the key dynamical processes supporting the 21.7 Zhengzhou Record-breaking hourly rainfall in China. Adv. Atmos. Sci. 40, 337–349. https://doi.org/10.1007/s00376-022-2061-y.

Wu, L., Huang, R., He, H., Shao, Y., Wen, Z., 2010. Synoptic characteristics of heavy rainfall events in pre-monsoon season in South China. Adv. Atmos. Sci. 27, 315–327. https://doi.org/10.1007/s00376-009-8219-z.

Xu, X., Li, L., Zhang, Q., Fan, Z., 2024. Understanding simulated causes of damaging surface winds in a Derecho-producing mesoscale convective system near the East China Coast based on convection-permitting simulations. Adv. Atmos. Sci. 41, 2112–2130. https://doi.org/10.1007/s00376-024-3314-8.

Yamazaki, M., Jemcov, A., Sakaue, H., 2021. A review on the current status of icing physics and mitigation in aviation. Aerospace 8, 188. https://doi.org/10.3390/aerospace8070188.

Yang, N., Zhu, K., Xue, M., 2022. Investigation of the convection-allowing prediction error of an extreme precipitation event of China using CRTM-simulated brightness temperature. J. Geophys. Res. Atmos. 127, e2022JD036760. https://doi.org/10.1029/2022JD036760.

Yuan, M., Lv, A., Wang, W., Dong, X., Ping, F., 2025. The microphysical properties and processes in in-flight icing: a case study. Atmos. Res. 326, 108326. https://doi.org/10.1016/j.atmosres.2025.108326.

Yum, S.S., Hudson, J.G., 2002. Maritime/continental microphysical contrasts in stratus. Tellus Ser. B Chem. Phys. Meteorol. 54, 61–73. https://doi.org/10.3402/tellusb.v54i1.16648.

Zeng, T., Wang, Z., Chen, Y., 2022. Calculation method of SLD collection efficiency for three-dimensional complex configuration. In: *International Conference on Mechanical Design and Simulation (MDS 2022)*, Vol. 12261 of, International Conference on Mechanical Design and Simulation (MDS 2022). SPIE, pp. 1088–1100. https://doi.org/10.1117/12.2638757.

Zhuge, X., Coauthors, 2024. Introduction to the NJIAS Himawari-8/9 cloud feature dataset for climate and typhoon research. Earth Syst. Sci. Data 16, 1747–1769. https://doi.org/10.5194/essd-16-1747-2024.

Zhuge, X., Zou, X., Li, X., Tang, F., Yao, B., Yu, L., 2021. Seasonal and diurnal variations in cloud-top phase over the Western North Pacific during 2017-2019. Remote Sens. 13. https://doi.org/10.3390/rs13091687.

Ziegler, C.L., 1985. Retrieval of thermal and microphysical variables in observed convective storms. Part 1: Model development and preliminary testing. J. Atmos. Sci. 42, 1487–1509. https://doi.org/10.1175/1520-0469(1985)042<1487:ROTAMV>2.0.CO;2.